

Luminosity-duration relations and luminosity functions of repeating and non-repeating fast radio bursts

Tetsuya Hashimoto,^{1,2*} Tomotsugu Goto,¹ Ting-Wen Wang,¹ Seong Jin Kim,¹ Simon C.-C. Ho,¹ Alvina Y. L. On,^{1,2,3} Ting-Yi Lu,¹ and Daryl Joe D. Santos¹

¹*Institute of Astronomy, National Tsing Hua University, 101, Section 2, Kuang-Fu Road, Hsinchu, 30013, Taiwan (R.O.C.)*

²*Centre for Informatics and Computation in Astronomy (CICA), National Tsing Hua University, 101, Section 2, Kuang-Fu Road, Hsinchu, 30013, Taiwan (R.O.C.)*

³*Mullard Space Science Laboratory, University College London, Holmbury St Mary, Surrey RH5 6NT, UK*

Accepted 2020 March 27. Received 2020 March 27; in original form 2019 November 16

ABSTRACT

Fast radio bursts (FRBs) are mysterious radio bursts with a time scale of approximately milliseconds. Two populations of FRB, namely repeating and non-repeating FRBs, are observationally identified. However, the differences between these two and their origins are still cloaked in mystery. Here we show the time-integrated luminosity-duration (L_ν - $w_{\text{int,rest}}$) relations and luminosity functions (LFs) of repeating and non-repeating FRBs in the FRB Catalogue project. These two populations are obviously separated in the L_ν - $w_{\text{int,rest}}$ plane with distinct LFs, i.e., repeating FRBs have relatively fainter L_ν and longer $w_{\text{int,rest}}$ with a much lower LF. In contrast with non-repeating FRBs, repeating FRBs do not show any clear correlation between L_ν and $w_{\text{int,rest}}$. These results suggest essentially different physical origins of the two. The faint ends of the LFs of repeating and non-repeating FRBs are higher than volumetric occurrence rates of neutron-star mergers and accretion-induced collapse (AIC) of white dwarfs, and are consistent with those of soft gamma-ray repeaters (SGRs), type Ia supernovae, magnetars, and white-dwarf mergers. This indicates two possibilities: either (i) faint non-repeating FRBs originate in neutron-star mergers or AIC and are actually repeating during the lifetime of the progenitor, or (ii) faint non-repeating FRBs originate in any of SGRs, type Ia supernovae, magnetars, and white-dwarf mergers. The bright ends of LFs of repeating and non-repeating FRBs are lower than any candidates of progenitors, suggesting that bright FRBs are produced from a very small fraction of the progenitors regardless of the repetition. Otherwise, they might originate in unknown progenitors.

Key words: radio continuum: transients – stars: magnetars – stars: magnetic field – stars: neutron – (stars:) binaries: general – stars: luminosity function, mass function

1 INTRODUCTION

Since the first discovery of a fast radio burst (FRB; Lorimer et al. 2007), ~100 FRBs have been detected to date (e.g., Petroff et al. 2016). There are two different types of FRBs: repeating and non-repeating FRBs. The first repeating burst was named FRB 121102 (Spitler et al. 2016). The repeating signals of FRB 121102 have been confirmed more than 100 times until now (Spitler et al. 2016; Scholz et al. 2016; Spitler et al. 2018; Michilli et al. 2018; Zhang et al. 2018). Recently, repeating FRBs have been discovered increasingly

by the Canadian Hydrogen Intensity Mapping Experiment (CHIME; CHIME/FRB Collaboration et al. 2019b,a,c) and the Robert C. Byrd Green Bank Telescope (GBT; Kumar et al. 2019). In spite of the observational progress, the differences between repeating and non-repeating FRBs are still unclear because of observational limitations. If a typical repeating time scale is longer than observational time scales or the luminosities of repeated bursts are too faint, such repeats can not be detected by current radio telescopes. Thus, the FRBs may be mistakenly recognised as non-repeating FRBs. A significant fraction of repeating FRBs might contaminate non-repeating FRBs. In this sense, these two categories do not necessarily indicate two different origins. In fact a vol-

* E-mail: tetsuya@phys.nthu.edu.tw

umetric occurrence rate, i.e., how many FRBs happen per unit time per unit volume, of nearby non-repeating FRBs exceeds those of possible progenitor candidates (Ravi 2019). This suggests that at least some fractions of non-repeating FRBs originate from progenitors that emit multiple bursts over their lifetimes.

On the other hand, another FRB named FRB 171019 was originally considered as a non-repeating FRB. However, two repetitions of radio bursts happened from this source and were reported recently (Kumar et al. 2019). Therefore, a comparison of physical properties of repeating and non-repeating FRBs is one of the most important tasks to understand what makes this phenomenal difference. Recently, CHIME/FRB Collaboration et al. (2019c) reported that the observed duration of repeating FRBs detected by CHIME is longer than that of non-repeating FRBs, suggesting different populations between repeating and non-repeating FRBs.

Theoretical models of the origins of FRBs are in chaos. So far ~50 physical models of FRBs have been proposed (e.g., Platts et al. 2019). There is no consensus yet on the physical origins of repeating and non-repeating FRBs. There were some observational efforts to find FRBs at the positions of possible progenitors, e.g., remnants of super-luminous supernovae (Law et al. 2019) and gamma-ray bursts (GRBs; Madison et al. 2019; Men et al. 2019). However, there is so far no direct detection of FRBs from these possible progenitors. Multi-wavelength and multi-messenger observations at the locations of FRBs were also conducted (e.g., Callister et al. 2016; MAGIC Collaboration et al. 2018; Sun et al. 2019; Martone et al. 2019; Tingay & Yang 2019; Aartsen et al. 2020) with no clear detection of counterparts.

One way to constrain FRB origins is a luminosity-duration relation of FRBs. Hashimoto et al. (2019) found an unexpected positive correlation between the time-integrated luminosity, L_ν , and rest-frame intrinsic duration, $w_{\text{rest,int}}$, for non-repeating FRBs (see Sections 3.1 and 3.2 for exact definitions of L_ν and $w_{\text{rest,int}}$, respectively). They argued that physical models which explicitly predict the correlation would be favoured for non-repeating FRBs.

In this paper, we compare repeating and non-repeating FRBs in the L_ν - $w_{\text{int,rest}}$ parameter space and in luminosity functions. The structure of the paper is as follows: we describe a compilation of our FRB sample in Section 2. In Section 3, we demonstrate calculations of L_ν , $w_{\text{int,rest}}$, and luminosity functions. Results of the L_ν - $w_{\text{int,rest}}$ relations and luminosity functions are described in Section 4. The implications of our results on repeating and non-repeating FRB populations and their origins are discussed in Section 5 followed by conclusions in Section 6. Throughout the paper, we assume the *Planck15* cosmology (Planck Collaboration et al. 2016) as a fiducial model, i.e., Λ cold dark matter cosmology with $(\Omega_m, \Omega_\Lambda, \Omega_b, h) = (0.307, 0.693, 0.0486, 0.677)$, unless otherwise mentioned.

2 SAMPLE

We compiled 90 ‘verified’ FRBs from the FRB Catalogue (FRBCAT) project¹ (Petroff et al. 2016) as of 21 August

2019, which were confirmed through publication, or received with high importance scores in the VOEvent Network. The original FRBCAT catalogue contains FRB ID, telescope, galactic latitude (b), longitude (l), sampling time (w_{sample}), central frequency (ν_{obs}), observed dispersion measure (DM_{obs}), observed burst duration (w_{obs}), and observed fluence ($E_{\nu_{\text{obs}}}$) together with errors of these observed parameters. In cases where the $E_{\nu_{\text{obs}}}$ error, $\delta E_{\nu_{\text{obs}}}$, is not provided in literature, we calculated it using

$$\delta E_{\nu_{\text{obs}}} = E_{\nu_{\text{obs}}} \{ (\delta w_{\text{obs}}/w_{\text{obs}})^2 + (\delta F_{\text{obs}}/F_{\text{obs}})^2 \}^{1/2}, \quad (1)$$

where δw_{obs} , δF_{obs} , and F_{obs} are w_{obs} error, observed flux density error, and observed flux density, respectively.

If δw_{obs} is not provided in literature, we assumed 10% uncertainty, i.e., $\delta w_{\text{obs}}/w_{\text{obs}} = 0.1$. We adopted this value because the median of $\delta w_{\text{obs}}/w_{\text{obs}}$ is ~0.1 in our sample.

If δF_{obs} is not given in literature, we assumed δF_{obs} to be telescope-dependent. Among 90 verified FRBs catalogued in FRBCAT, 10 FRBs do not have δF_{obs} : one Arecibo, three Pushchino, four UTMOST, one CHIME, and one DSA-10 FRBs. The assumed fractional uncertainties, $\delta F_{\text{obs}}/F_{\text{obs}}$, are 6, 0.3, and 0.5 for Arecibo, UTMOST, and CHIME, respectively. These values are empirically determined for individual telescopes by calculating median values of $\delta F_{\text{obs}}/F_{\text{obs}}$ reported in the FRBCAT project. We caution readers that these fractional uncertainties are subjected to various uncertainties. For example, if the slope of the source counts is much flatter than $\alpha_{\text{SC}} \lesssim 1.1$, the deviations from the published values might be large. However, since the accurate value of α_{SC} is still unknown, the empirically estimated uncertainties might be updated once more accurate measurements become available. The fluence uncertainties of FRBs detected with Pushchino are not explicitly reported (Fedorova & Rodin 2019). We assumed a conservative fractional uncertainty of 0.5 for Pushchino FRBs, while the signal-to-noise ratios of the FRBs are 6.2, 9.1, and 8.3 (Fedorova & Rodin 2019). These signal-to-noise ratios of Pushchino FRBs are systematically lower than those of FRBs detected with other telescopes. In this regard, Pushchino FRBs are not used in calculating the luminosity functions in Section 3.4. The fluence uncertainty of DSA-10 is assumed to be 10% since the observed fluence exceeded 8σ detection limit by ~15% with an accurate localisation within the field of view (Ravi et al. 2019).

The reported fluences of FRBs detected with Parkes, CHIME and UTMOST are actually lower limits because the burst locations with respect to the beam centre are unknown. Individual fluence corrections for the positional uncertainties are difficult for such FRBs. This uncertainty is statistically included in the calculations of the luminosity function of each telescope in Section 3.4. We do not include this uncertainty in the ASKAP luminosity function because ASKAP is not affected by this uncertainty.

Intra-channel bandwidth, $\Delta\nu_{\text{obs}}$, is compiled from references therein, which is necessary for calculation of dispersion smearing. Spectral index, α , is also compiled from references therein if available, otherwise we assumed a mean value of $\alpha = -1.5$ (Macquart et al. 2019), where $E_{\nu_{\text{obs}}} \propto \nu_{\text{obs}}^\alpha$.

In order to treat irregular cases, we added four flags in the catalogue including ‘scattering flag’, ‘repeating flag’, ‘intrinsic-duration flag’, and ‘spec-z flag’. The scattering flag indicates the contamination of scattering broadening

¹ <http://frbcatalog.org/>

to w_{obs} . We rely on the estimates in literature and FRBCAT to determine the scattering flag. This flag is off when w_{obs} is reported after the deconvolution of the scattering tail (e.g., Shannon et al. 2018; CHIME/FRB Collaboration et al. 2019a,c). The repeating flag indicates confirmed repeating FRBs (e.g., Spitler et al. 2016; CHIME/FRB Collaboration et al. 2019b,c; Kumar et al. 2019). The intrinsic-duration flag is on if the reported burst duration is already corrected for instrumental and scattering broadening effects (CHIME/FRB Collaboration et al. 2019a). In such cases, we adopt the reported duration as an intrinsic duration, w_{int} , instead of our calculation. The spec- z flag is for four FRBs with spectroscopic redshift measured from the host galaxies (FRB 121102, 180916.J0158+65, 180924, and 190523; Tendulkar et al. 2017; Marcote et al. 2020; Bannister et al. 2019; Ravi et al. 2019). For these four FRBs we use the spectroscopic redshifts instead of the redshift estimated from the dispersion measure. Recently another host galaxy was identified (FRB 181112 host; Prochaska et al. 2019). This burst is not included in this work, since the burst information has not been listed in the FRBCAT as of 21 August 2019.

In the current FRBCAT, some of the individual bursts of repeating FRBs are incomplete. To supply the missing bursts, we compiled all of the parameters described above for each burst of repeating FRBs reported in other literature, i.e., 11 Arecibo repeats (Spitler et al. 2016), 5 GBT and 1 Arecibo (Scholz et al. 2016), and 93 GBT (Zhang et al. 2018) for FRB 121102, 6 CHIME repeats for FRB 180814.J0422+73 (CHIME/FRB Collaboration et al. 2019a,b), 2-10 CHIME repeats for 8 FRBs (CHIME/FRB Collaboration et al. 2019c), and 1 ASKAP and 2 GBT repeats for FRB 171019 (Kumar et al. 2019).

If spec- z is not available, we excluded FRBs with dispersion measures dominated by the Milky Way and halo contribution, i.e., $\text{DM}_{\text{obs}} - \text{DM}_{\text{MW}} - \text{DM}_{\text{halo}} \leq 0$, where DM_{MW} is a dispersion measure contributed by the interstellar medium in the Milky Way and DM_{halo} is a contribution from the dark matter halo hosting the Milky Way (see Section 3 for details). This is because the uncertainties of redshift and distance are too large to calculate the luminosity.

After applying this criterion, our sample includes a total of 11 repeating FRBs with 144 repeats and 77 non-repeating FRBs.

3 ANALYSIS

3.1 Time-integrated luminosity

We calculated a time-integrated luminosity and rest-frame intrinsic duration of our FRB sample in a similar way to Hashimoto et al. (2019). Here we briefly describe the process. We assumed YMW16 electron-density model (Yao et al. 2017) to estimate DM_{MW} . The DM_{MW} was accumulated up to 10 kpc along the line of sight to FRBs. Dispersion measures contributed from FRB host galaxies, DM_{host} , were parameterised as $\text{DM}_{\text{host}} = 50.0/(1+z)$ pc cm⁻³ following Shannon et al. (2018). There are several studies in which DM_{halo} are investigated (e.g., Dolag et al. 2015; Prochaska & Zheng 2019; Keating & Pen 2020). We assumed $\text{DM}_{\text{halo}} = 65$ pc cm⁻³, which is a mean between 50 and 80 pc cm⁻³ (Prochaska & Zheng 2019). After sub-

tracting DM_{MW} , DM_{halo} , and DM_{host} from DM_{obs} , the remaining term is a contribution from inter-galactic medium, DM_{IGM} . While DM_{IGM} should fluctuate along different line of sights, the mean value of DM_{IGM} is expressed as a function of redshift with some cosmological parameters (e.g., Zhou et al. 2014). By assuming the cosmological parameters, redshift is roughly estimated from $\text{DM}_{\text{IGM}}(z)$ with uncertainties originated from the line-of-sight fluctuation of DM_{IGM} and DM_{obs} error, $\delta\text{DM}_{\text{obs}}$. As a conservative estimate, we adopted the highest uncertainty of $\text{DM}_{\text{IGM}}(z)$, $\delta\text{DM}_{\text{IGM}}(z)$, among simulations with different resolutions (Zhu et al. 2018). We used spectroscopic redshift instead of DM-derived redshift if available (i.e., FRB121102, 180916.J0158+65, 180924, and 190523: Tendulkar et al. 2017; Marcote et al. 2020; Bannister et al. 2019; Ravi et al. 2019). We calculated time-integrated luminosities of FRBs at rest-frame 1.83 GHz by using Eq. 6 in Hashimoto et al. (2019). This rest-frame frequency is selected so that the K -correction term in Eq. 6, $\frac{1}{(1+z)^{2+\alpha}} \left(\frac{\nu_{\text{rest}}}{\nu_{\text{obs}}} \right)^\alpha$, can be minimised. We note that a spectral index, $\alpha = -1.5$ (Macquart et al. 2019), is assumed for FRBs without α measurement.

3.2 Rest-frame intrinsic duration

In general, FRB pulse duration is broadened by dispersion smearing, data sampling time interval, and scattering. The dispersion smearing is caused by a finite spectral resolution of the instrument. The pulse delay within the observational spectral resolution broadens the observed duration. The instrumental sampling time also causes pulse broadening. To derive the intrinsic duration of FRBs (w_{int}), we removed these two instrumental effects on pulse broadening by following Eq. 5 in Hashimoto et al. (2019). In the case when w_{int} is not instrumentally resolved, i.e., $w_{\text{obs}}^2 \leq w_{\text{sample}}^2 + w_{\text{DM}}^2$, we use w_{obs} as the upper limit of w_{int} , where w_{DM} is the pulse broadening by dispersion smearing. Note that scattering broadening is not explicitly removed in this work except for some cases in which deconvoluted duration is reported in the literature (e.g., Shannon et al. 2018; CHIME/FRB Collaboration et al. 2019a,c). Instead of the deconvolution, we flagged the scattering feature. Therefore, the intrinsic duration of FRBs with scattering flags could be shorter than the reported values. The rest-frame intrinsic duration, $w_{\text{int,rest}}$, was calculated as $w_{\text{int,rest}} = w_{\text{int}}/(1+z)$.

Histograms of cumulative fractions of observed, instrumental, and derived parameters of our sample are summarised in Fig. 1. In the histograms, each sample is binned into 10 subsamples ranging from the minimum and maximum values. Cumulative histograms of DM_{IGM} and redshift for each telescope are shown in Figs. A1 and A2, respectively, in Appendix A. Monte Carlo simulations were performed to calculate errors of L_ν and $w_{\text{int,rest}}$ by independently assigning random 10,000 errors to DM_{obs} , w_{obs} , $\text{DM}_{\text{IGM}}(z)$, and $E_{\nu_{\text{obs}}}$. Here, the line-of-sight fluctuation of DM_{IGM} mentioned above is included in the error of $\text{DM}_{\text{IGM}}(z)$. Each random error is assumed to follow a Gaussian probability distribution function with a standard deviation of the observational uncertainty.

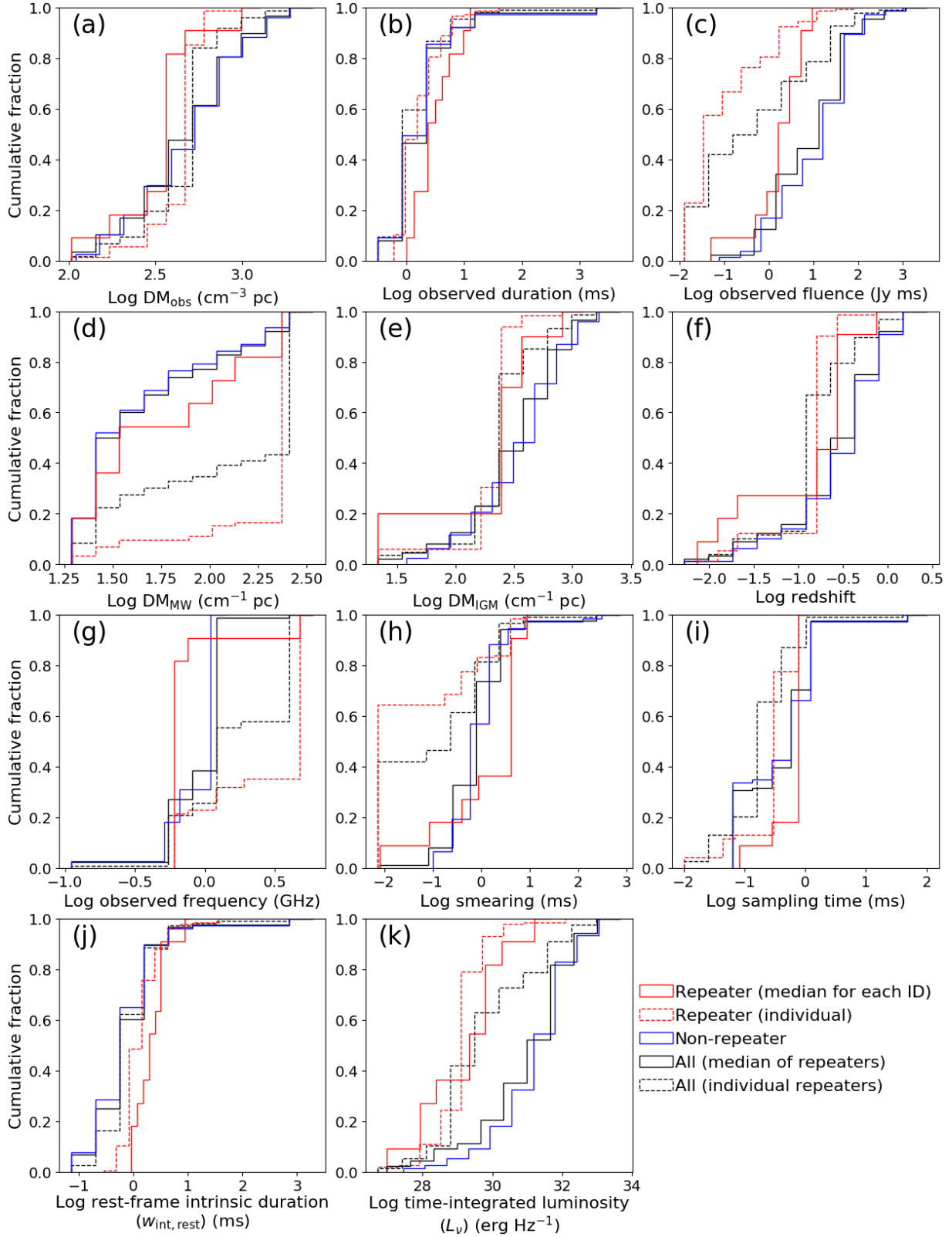


Figure 1. Cumulative fractions as a function of parameters of our FRB sample. From (a) to (k), the cumulative histograms are for observed dispersion measure, observed duration, observed fluence, dispersion measure of the Milky Way, dispersion measure of inter-galactic medium, redshift, observed frequency, dispersion smearing, instrumental sampling time, rest-frame intrinsic duration, and time-integrated luminosity at rest-frame 1.83 GHz. Black, red, and blue lines correspond to the total sample, repeating FRBs, and non-repeating FRBs, respectively. Solid black and red lines include repeating FRBs counted such that an identical FRB ID is single source with median values of parameters among the repeats, e.g., FRB 121102 is counted as one FRB. Dashed lines include repeats individually counted for each repeating FRB, e.g., FRB 121102 is counted as 110 FRBs. Note that upper limits are included in the histogram of the (j) rest-frame intrinsic duration. Cumulative histograms of DM_{IGM} and redshift for each telescope are shown in Figs. A1 and A2, respectively, in Appendix A.

3.3 Rest-frame cadences of repeating FRBs

We also calculated rest-frame cadences of repeating FRBs. The rest-frame cadence is calculated as $N_{\text{repeat}}(1+z)/t_{\text{obs}}$, where N_{repeat} is the number of repeats of each FRB and t_{obs} is the observed time on source. The values of N_{repeat} , t_{obs} , and references of 11 repeating FRBs in our sample are summarised in Table 1.

3.4 Calculation of luminosity function

Here, we calculate the FRB luminosity functions for each telescope, because different telescopes have different sensitivities and survey volumes. For this purpose we divided our sample into subsamples detected with the same telescope. We only consider FRBs at $0.01 \leq z < 0.7$ to calculate the luminosity functions. The upper limit could mitigate a possible volumetric density evolution of progenitors with redshift (e.g., Hashimoto et al. 2020b in prep.). The lower limit is applied to exclude very close events that could involve huge uncertainties on the DM-derived distances (see also discussion in Section 5.3). The upper limit is shown by a dashed vertical line in Fig. 2. Table 2 and 3 summarise the number of FRBs (repeating and non-repeating, respectively) observed with each telescope in our sample. The CHIME detections of repeating FRBs are used to derive the luminosity function of repeating FRBs. The repeating FRBs observed with GBT and Arecibo are also included in our analysis to constrain the upper limit of the luminosity function. As for non-repeating FRBs, only Parkes, ASKAP, CHIME, and UTMOST observations are considered to derive luminosity functions because of the small statistics of other telescopes.

To estimate the luminosity functions of FRBs, we use a simple V_{max} method (e.g., Schmidt 1968; Avni & Bahcall 1980), where the 4π coverage of V_{max} ($V_{\text{max},4\pi}$) is expressed as

$$V_{\text{max},4\pi} = \frac{4\pi}{3}(d_{\text{max}}^3 - d_{\text{min}}^3). \quad (2)$$

Here d_{min} is a comoving distance to $z = 0.01$, which is the lower redshift limit applied to our sample. d_{max} is a maximum comoving distance for a FRB with a time-integrated luminosity, $L_{V_{\text{rest}}}$, to be detected with a specific fluence limit, E_{lim} . In previous studies, E_{lim} is reported in terms of E_V for Parkes and UTMOST (Keane & Petroff 2015; Caleb et al. 2016) and in terms of $E_V \times w_{\text{obs}}^{1/2}$ for ASKAP, CHIME, and Arecibo (Shannon et al. 2018; CHIME/FRB Collaboration et al. 2019a; Spitler et al. 2014). To avoid systematic offsets in the luminosity functions due to the different definitions of E_{lim} , we empirically derived E_{lim} for each telescope with the same definition described in Appendix B. The value of E_{lim} is approximated by the peak of the data distributed along the perpendicular direction to the $w_{\text{obs}}^{1/2}$ dependency in the $E_{V_{\text{obs}}}$ - w_{obs} space, such that the duration dependency can be taken into account. The data distribution and histograms in the $E_{V_{\text{obs}}}$ - w_{obs} space of our sample are shown in Figs. B1 and B2. The adopted E_{lim} are summarised in Tables 2 and 3. By using Eq. 6 in Hashimoto et al. (2019), d_{max} is expressed as

$$d_{\text{max}}(z_{\text{max}}) = \left\{ \frac{L_{V_{\text{rest}}}(1+z_{\text{max}})^{2+\alpha}}{4\pi E_{\text{lim}}} \left(\frac{v_{\text{obs}}}{v_{\text{rest}}} \right)^\alpha \right\}^{1/2} (1+z_{\text{max}})^{-1}, \quad (3)$$

where z_{max} is redshift at the comoving distance of d_{max} .

We adopt the rest-frame frequency, ν_{rest} , at 1.83 GHz (Hashimoto et al. 2019). Since the left term of Eq. 3, comoving distance, is calculated with a cosmological assumption, the solution to z_{max} of the Eq. 3 provides individual FRBs with d_{max} . Note that we adopted $z_{\text{max}} = 0.7$ if the solution is higher than 0.7, so that z_{max} can not exceed the redshift cut, $z < 0.7$. Based on Eq. 2 and 3, we calculated $V_{\text{max},4\pi}$ of individual FRBs.

Each FRB was detected in a comoving volume of $V_{\text{max},4\pi} \times \Omega_{\text{sky}}$ during rest-frame survey time, $t_{\text{rest}} = t_{\text{obs}}/(1+z_{\text{FRB}})$, where Ω_{sky} and z_{FRB} are a fractional sky coverage of the survey and redshift of the FRB, respectively. Therefore, the number density of each FRB per unit time, $\rho(L_{V_{\text{rest}}})$, is

$$\rho(L_{V_{\text{rest}}}) = 1/(V_{\text{max},4\pi} \Omega_{\text{sky}} t_{\text{rest}}) = (1+z_{\text{FRB}})/(V_{\text{max},4\pi} \Omega_{\text{sky}} t_{\text{obs}}). \quad (4)$$

Each survey provides a different value of $\Omega_{\text{sky}} t_{\text{obs}}$. When FRBs are detected via multiple surveys, $\Omega_{\text{sky}} t_{\text{obs}}$ was accumulated for each telescope as follows.

$$\rho(L_{V_{\text{rest}}}) = (1+z_{\text{FRB}})/(V_{\text{max},4\pi} \Sigma_i \Omega_{\text{sky},i} t_{\text{obs},i}), \quad (5)$$

where i denotes i th survey with the same telescope. The adopted E_{lim} , $\Omega_{\text{sky},i} t_{\text{obs},i}$, and their references are summarised in Table 2 and 3.

Each telescope sample was divided into three luminosity bins, L_j ($j = 1, 2, 3$), in logarithmic scale (Fig. 3). Here we use the three bins in order to secure a meaningful number of samples in each bin. Within the luminosity bins, $\rho(L_j)$ is summed to derive luminosity function, Φ , i.e.,

$$\Phi(L_j) = \Sigma_k \rho(L_{j,k}) / \Delta \log L, \quad (6)$$

where the subscript k denotes the k th FRB in L_j bin and $\Delta \log L$ is the luminosity bin size. Note that the number of luminosity bins for CHIME/GBT and Arecibo repeating FRBs (median case) are adopted to be two and one, respectively, due to their small statistics.

With respect to the unknown positions of FRBs within the fields of view of Parkes, CHIME and UTMOST, Macquart & Ekers (2018) reported that the averaged fluence can vary by a factor of 1.7 depending on the slope of the source counts, α_{SC} . Considering that the reported fluences for Parkes, CHIME, and UTMOST are lower limits, we included this factor as a systematic uncertainty of fluence and thus time-integrated luminosity in the luminosity functions. The effective survey area in Table 3 also depends on α_{SC} (Macquart & Ekers 2018). In order to accurately estimate the dependency, α_{SC} and beam pattern have to be correctly calculated for each telescope. Such extensive analysis is out of scope of this paper. Macquart & Ekers (2018) reported that the effective survey area can increase by a factor of ~ 3 depending on α_{SC} . Instead of carrying out an extensive analysis, we included the factor of 3 as a systematic uncertainty on the survey area when the luminosity functions are calculated.

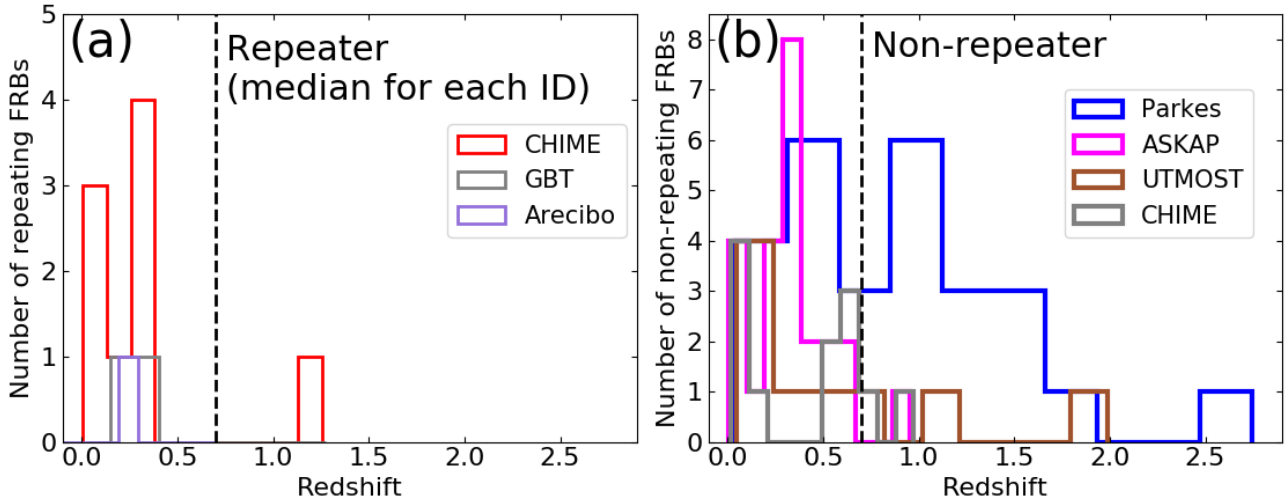
In summary, we used FRBs satisfying the following criteria for the calculations of luminosity functions:

- $0.01 \leq \text{redshift (spec-}z \text{ if available)} < 0.7$
- $E_{V_{\text{obs}}} \geq E_{\text{lim}}$

The sample for luminosity functions includes a total of 7 repeating FRBs with 87 repeats and 46 non-repeating FRBs.

Table 1. Number of repeats of each repeating FRB and observed time.

ID	N_{repeat}	t_{obs} (hour)	Reference
121102	110	84.1	Scholz et al. (2016); Zhang et al. (2018)
171019	3	1009.6	Kumar et al. (2019)
180814.J0422+73	6	23	CHIME/FRB Collaboration et al. (2019b,a)
180916.J0158+65	10	23 ± 8	CHIME/FRB Collaboration et al. (2019c)
181017.J1705+68	2	20 ± 11	CHIME/FRB Collaboration et al. (2019c)
181030.J1054+73	2	46 ± 18	CHIME/FRB Collaboration et al. (2019c)
181119.J12+65	3	19 ± 9	CHIME/FRB Collaboration et al. (2019c)
181128.J0456+63	2	16 ± 10	CHIME/FRB Collaboration et al. (2019c)
190116.J1249+27	2	8 ± 5	CHIME/FRB Collaboration et al. (2019c)
190209.J0937+77	2	62 ± 26	CHIME/FRB Collaboration et al. (2019c)
190222.J2052+69	2	20 ± 10	CHIME/FRB Collaboration et al. (2019c)

**Figure 2.** (Left) Redshift distributions of repeating FRBs detected by CHIME, GBT, and Arecibo. The number of repeating FRBs are counted such that the identical FRB ID is the single source. Here we use median redshift of repeats for each repeating FRBs. Dashed vertical line, $z = 0.7$, is the redshift cutoff applied to calculations of the luminosity functions. (Right) Same as left except for non-repeating FRBs detected by Parkes, ASKAP, UTMOST, and CHIME. All of our sample is shown before applying the redshift cuts and detection limits for the calculations of luminosity functions.**Table 2.** Total number of repeating FRBs observed with each telescope in our sample and individual survey parameters.

Repeating FRBs					
Telescope	Number ^a (all)	Number ^a ($0.01 \leq z < 0.7$ and $E_{\nu_{\text{obs}}} \geq E_{\text{lim}}$)	E_{lim} ^d (Jy ms)	$\Omega_{\text{sky},i} t_{\text{obs},i}$ ^e (deg ² hour)	$\Omega_{\text{sky},i} t_{\text{obs},i}$ reference
CHIME	9 (31)	5 (15) ^c	$1.7 w_{\text{obs}}^{1/2}$	1.39×10^6	CHIME/FRB Collaboration et al. (2019c,b)
GBT ^b	2 (100)	2 (63) ^c	$0.032 w_{\text{obs}}^{1/2}$	1.25	Scholz et al. (2016)
				0.28	Zhang et al. (2018)
				0.58	Kumar et al. (2019)
Arecibo ^b	1 (12)	1 (9) ^c	$0.052 w_{\text{obs}}^{1/2}$	6.23	Spitler et al. (2014)
				0.23	Spitler et al. (2016)
ASKAP ^b	1 (1)	1(1)			

^a Repeating FRBs are counted such that the identical FRB ID is the single source. Numbers in parentheses are individual counts of repeats. Note that a few repeating FRBs were detected in multiple telescopes. ^b Observations were targeted to repeating FRBs, which places upper limits on FRB number densities and luminosity functions. ^c FRBs used for the calculations of luminosity functions. ^d Detection limit, E_{lim} , is approximated by a peak of data distribution along the perpendicular direction to the $w_{\text{obs}}^{1/2}$ (ms^{1/2}) dependency in the $E_{\nu_{\text{obs}}}$ - w_{obs} space (see Appendix B). ^e Survey area times exposure time on sky.

Table 3. Total number of non-repeating FRBs observed with each telescope in our sample and individual survey parameters.

Non-repeating FRBs					
Telescope	Number (all)	Number ($0.01 \leq z < 0.7$ and $E_{\nu_{\text{obs}}} \geq E_{\text{lim}}$)	E_{lim}^b (Jy ms)	$\Omega_{\text{sky}, i} t_{\text{obs}, i}$ (deg ² hour)	$\Omega_{\text{sky}, i} t_{\text{obs}, i}$ reference
Parkes	27	10 ^a	$0.72 w_{\text{obs}}^{1/2}$	267 4394.5	Zhang et al. (2019) Osłowski et al. (2019)
ASKAP	24	20 ^a	$28 w_{\text{obs}}^{1/2}$	1.32×10^4 5.1×10^5 1.36×10^4 255	Bannister et al. (2017) Shannon et al. (2018) Macquart et al. (2019) Bannister et al. (2019)
CHIME	12	10 ^a	$1.7 w_{\text{obs}}^{1/2}$	$< 2.83 \times 10^4$	CHIME/FRB Collaboration et al. (2019a)
UTMOST	9	6 ^a	$13 w_{\text{obs}}^{1/2}$	2.58×10^4 7.43×10^4	Caleb et al. (2017) Farah et al. (2019)
Pushchino	2	-			
DSA-10	1	-			
GBT	1	1			
Arecibo	1	1			

^a FRBs used for the calculations of luminosity functions. ^b Detection limit, E_{lim} , is approximated by a peak of data distribution along the perpendicular direction to the $w_{\text{obs}}^{1/2}$ (ms^{1/2}) dependency in the $E_{\nu_{\text{obs}}}$ - w_{obs} space (see Appendix B).

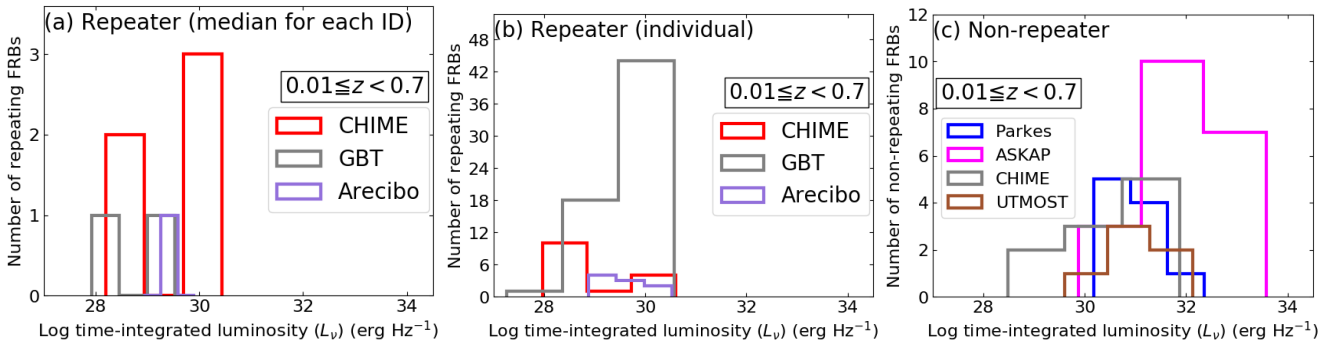


Figure 3. (Left) Histograms of the time-integrated luminosities at rest-frame 1.83 GHz of repeating FRBs. Repeating FRBs are counted such that the identical FRB ID is the single source. (Middle) Same as left except for counting repeats individually for each repeating FRB. (Right) Same as left except for non-repeating FRBs. Only FRBs used for the calculations of luminosity functions are demonstrated.

4 RESULTS

4.1 Luminosity-duration relation

Fig. 4 indicates rest-frame intrinsic duration, $w_{\text{int,rest}}$, as a function of time-integrated luminosity, L_ν , of FRBs. Repeating and non-repeating FRBs are shown by red and blue colours, respectively. In the left panel of Fig. 4, median values of repeating pulses of each FRB are shown in this parameter space (red stars), while individual repeats are shown in the right panel (red dots and triangles). We found that repeating FRBs occupy relatively fainter and longer duration compared with non-repeating ones in the L_ν - $w_{\text{int,rest}}$ space (see also Fig. 1).

Fig. 4 also indicates no clear correlation between L_ν and $w_{\text{int,rest}}$ for repeating FRBs. In contrast, we confirmed a positive correlation between L_ν and $w_{\text{int,rest}}$ of non-repeating FRBs (Hashimoto et al. 2019) except for some outliers with very long duration and faint luminosity. These results suggest different origins of repeating and non-repeating FRBs (see Section 5 for details).

Distribution of repeating FRBs in a grey shaded region

in Fig. 4b is magnified in Fig. 5. Different markers correspond to different repeating FRBs in Fig. 5. During repeats of FRBs, they move around in this parameter space. However, we do not find any clear trend in terms of L_ν and $w_{\text{int,rest}}$. This point is also confirmed in Fig. 6 that is demonstrated in offset distances from median coordinates of each repeating FRB in the L_ν - $w_{\text{int,rest}}$ plane.

4.2 Cadences of repeating FRBs as a function of luminosity

We also investigated rest-frame cadences of repeating FRBs as a function of time-integrated luminosity in Fig. 7. In Fig. 7, averaged repeating cadence of each repeating FRB is compared with median of L_ν . We found no clear correlation between these two parameters.

4.3 Luminosity function of FRBs

We show luminosity functions of repeating and non-repeating FRBs at $0.01 \leq z < 0.7$ in Fig. 8. The luminosity

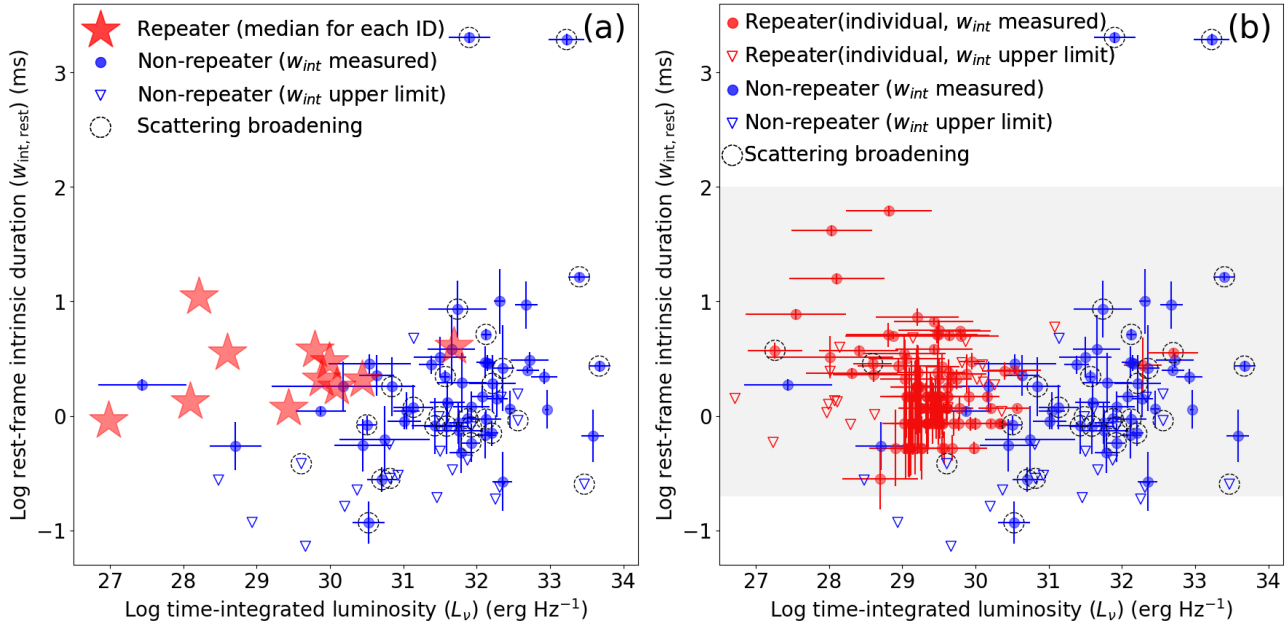


Figure 4. (Left) Rest-frame intrinsic duration as a function of time-integrated luminosity at rest-frame 1.83 GHz of FRBs. Red and blue colours are repeating and non-repeating FRBs, respectively. Each repeating FRB represents median values of the repeats. Upper limits on the rest-frame intrinsic duration are indicated by open triangles. FRBs with scattering broadening features are highlighted by dashed circles. Errors of L_ν and $w_{\text{int, rest}}$ are calculated by Monte Carlo simulations. Random 10,000 errors are independently assigned to DM_{obs} , w_{obs} , $\text{DM}_{\text{IGM}}(z)$, and $E_{\nu_{\text{obs}}}$, which follow Gaussian probability distribution functions with the observational uncertainties. The line-of-sight fluctuation of $\text{DM}_{\text{IGM}}(z)$ (Zhu et al. 2018) is included in the error of $\text{DM}_{\text{IGM}}(z)$. (Right) Same as left, except that the repeats of each repeating FRB are individually demonstrated. Grey shaded region is magnified in Fig. 5.

functions are independently calculated for repeating (stars) and non-repeating (dots) FRBs detected by different telescopes because of different survey parameters as shown in Table 2 and 3. The uncertainty in the time-integrated luminosity with respect to the unknown positions of FRBs is shown by upper shaded regions around the luminosity functions for Parkes, CHIME, and UTMOST. Lower shaded regions correspond to systematic uncertainties of the effective survey areas arising from the uncertainty in the slope of source counts, α_{SC} (see Section 3.4 for details).

Since the FRB luminosity function is dependent on the number density of progenitors and the event rate, there are two possible ways to count the number of repeating FRBs. One is by counting number of progenitors, i.e., one FRB ID corresponds to one FRB. Another is by counting number of repeats individually. The former is a fair way to count the number density of the progenitors unless repeating FRBs contaminate non-repeating sample significantly. The latter could be a fairer way to count the event rate if the non-repeating FRBs are significantly contaminated by the repeating ones.

In the left panel of Fig. 8, the number of repeating FRBs are counted such that the identical FRB ID is the single source, while in the right panel, repeats are counted individually for each FRB. GBT and Arecibo observations for repeating FRBs place upper limits on the luminosity functions (open grey and purple stars with arrows) since the observations were targeted on already known locations of repeating FRBs (Spitler et al. 2014, 2016; Scholz et al. 2016; Zhang et al. 2018; Kumar et al. 2019). CHIME observations for non-repeating FRBs place lower limits (open grey

dots with arrows) since only the upper limit on the survey volume is provided due to the pre-commissioning operation (CHIME/FRB Collaboration et al. 2019a).

In Fig. 8 left, in spite of different sensitivities and survey parameters, different telescopes provide roughly similar luminosity functions for non-repeating FRBs. The lower limits from CHIME non-repeating FRBs are consistent with other non-repeating luminosity functions.

The CHIME luminosity function of repeating FRBs in the left panel of Fig. 8 (red stars) clearly deviates from luminosity functions of non-repeating FRBs. This deviation is still obvious when the repeats are counted individually (right panel in Fig. 8). The difference in the luminosity functions imply that repeating and non-repeating FRBs are indeed different populations. In Fig. 8, we also found that the volumetric occurrence rates strongly depend on luminosity of FRBs regardless of the repetition. Bright FRBs are extremely rare compared to faint ones.

5 DISCUSSION

5.1 Luminosity function of FRBs in a previous study

Luo et al. (2018) calculated normalised luminosity functions of FRBs with assumptions of different types of host galaxies and DM_{MW} models by Cordes & Lazio (2002) and Yao et al. (2017). Their sample includes one repeating FRB 121102 and 32 non-repeating FRBs at $0.13 < z < 2.0$. They used isotropic luminosity integrated over the frequency in units of erg s^{-1} . In this work, a total of 7 repeating FRBs

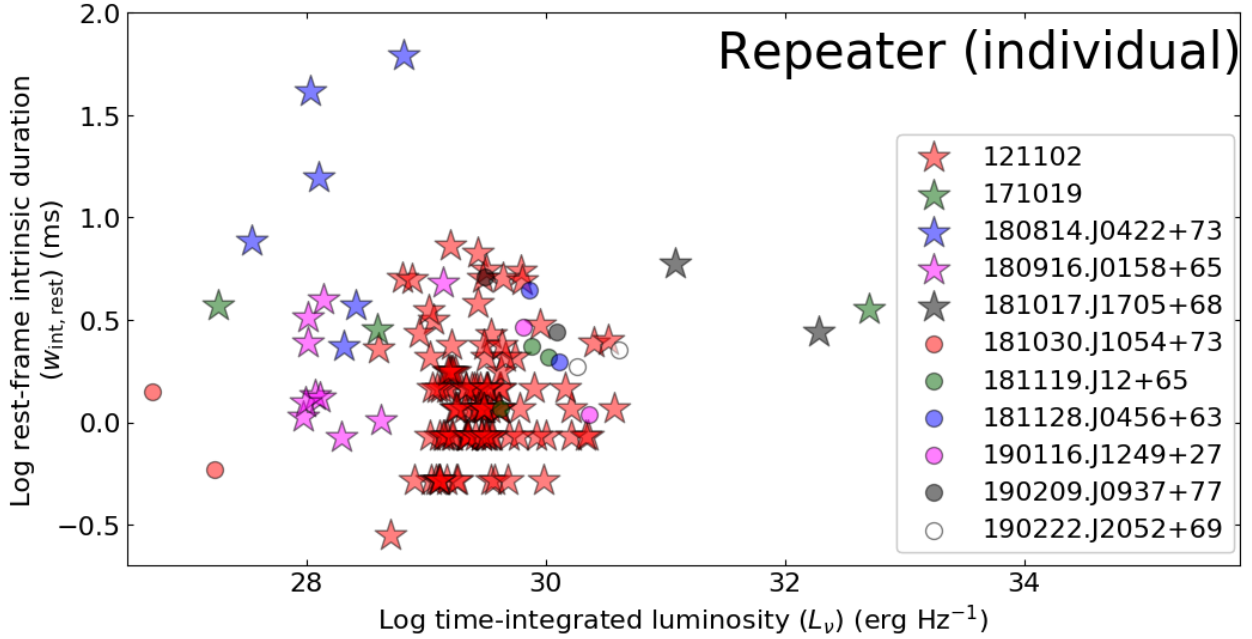


Figure 5. Magnified figure of the grey shaded region in Fig. 4(b). Only repeating FRBs are shown. Repeats from the same progenitor, i.e., the same FRB ID, are demonstrated by the same symbols listed in the legend.

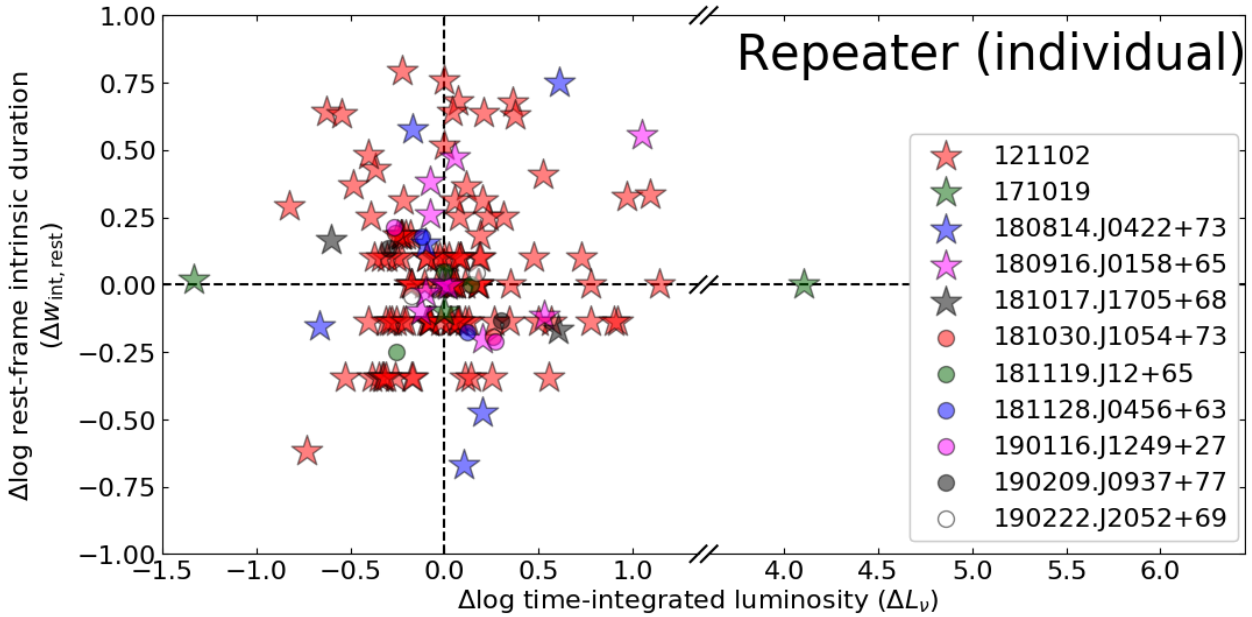


Figure 6. Same as Fig. 5 except for off-set axes from median coordinates of each repeating FRB in the L_ν - $w_{\text{int,rest}}$ parameter space.

and 46 non-repeating FRBs are used for the calculations of the luminosity functions. Our sample is limited to FRBs at $0.01 \leq z < 0.7$. The upper bound could reduce the possible effect of the redshift evolution (e.g., Hashimoto et al. 2020b in prep.). The lower bound could reduce the large uncertainty on distances to nearby FRBs. We use the time-integrated luminosity in units of erg Hz^{-1} without integration over the frequency. Due to these differences, the direct comparison between luminosity functions by Luo et al. (2018) and this work is not straightforward. Luo et al. (2018)

reported a power-law slope of the normalised luminosity functions ranging from $\alpha_{\text{LF}} = -1.8$ to -1.2 . We fitted the luminosity functions with power-law functions weighted by the inverted Poisson errors. The best-fit power-law slopes are $\alpha_{\text{LF}} = -2.5, -2.1$, and -1.0 for repeating FRBs (CHIME median for each ID), repeating FRBs (CHIME individual count), and non-repeating FRBs including Parkes, ASKAP, and UTMOST, respectively. Although Luo et al. (2018) reported a cutoff of the luminosity function at the bright end, we do not find any clear cutoff up to $\sim 10^{34} \text{ erg Hz}^{-1}$. This is

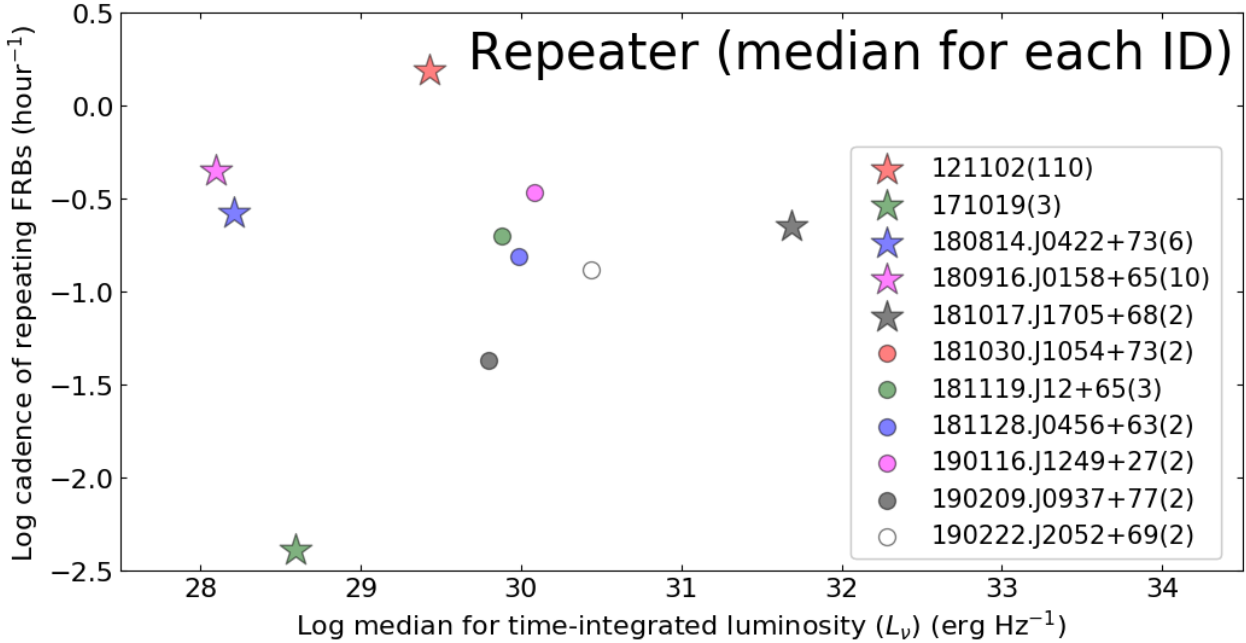


Figure 7. Averaged cadence as a function of median of time-integrated luminosity at rest-frame 1.83 GHz of repeating FRBs. Markers are the same as Fig. 6. Numbers in parentheses are the number of repeats for each repeating FRB.

probably because we do not assume any functional shape to calculate the luminosity functions. However, they assumed a Schechter luminosity function that includes a cutoff. We do not exclude the possibility of a cutoff beyond 10^{34} erg Hz $^{-1}$, where no FRB has been found in our sample. Shannon et al. (2018) suggested either a decreasing number of FRBs towards the bright end or a cutoff above 10^{34} erg Hz $^{-1}$ on the basis of ASKAP fly’s-eye survey data. The luminosity functions of non-repeating FRBs in this work (Fig. 8) decline towards the bright end of $\sim 10^{34}$ erg Hz $^{-1}$, confirming the point presented by Shannon et al. (2018) with better statistics including FRBs detected with other telescopes.

5.2 Astrophysical implications on FRB populations

Observationally, FRBs are divided into two categories: repeating and non-repeating. However, if only a single burst is detected among repeats due to low telescope sensitivity or long period between repeats, it may be recognised as a non-repeating FRB. Therefore non-repeating FRB could be significantly contaminated by repeating FRBs. In this sense these two categories do not necessarily indicate two different origins.

Ravi (2019) estimated lower limits on a volumetric occurrence rate of non-repeating FRBs detected by CHIME during the pre-commissioning phase. The lower limits actually depend on the assumed dispersion measures of host galaxies. In many cases, the lower limits exceed volumetric occurrence rates of possible progenitors of non-repeating FRBs, e.g., neutron-star merger and white-dwarf merger. This suggests that at least some fractions of non-repeating FRBs originate from sources that emit repeating bursts over their lifetimes.

We found that repeating and non-repeating FRBs oc-

cupy different parameter spaces in the L_ν - $w_{\text{int,rest}}$ plane in Fig. 4. Although several repeating FRBs overlap with non-repeating FRBs and vice versa, majorities of FRBs are clearly separated in Fig. 4. Repeating FRBs show relatively longer $w_{\text{int,rest}}$ on average and much fainter L_ν compared with those of non-repeating FRBs (Fig. 4 left). These differences are also demonstrated in Figs. 1(j) and (k). The cumulative histograms of repeating FRBs (red solid and dashed lines in Fig. 1) indicate longer $w_{\text{int,rest}}$ and fainter L_ν than those of non-repeating FRBs (blue solid lines in Fig. 1). We note that the difference in $w_{\text{int,rest}}$ is marginal, when individual repeats of repeating FRBs are compared with that of non-repeating FRBs. A difference in observed duration between repeating and non-repeating FRBs was reported by CHIME/FRB Collaboration et al. (2019c). We confirmed it with a more physically motivated parameter, $w_{\text{int,rest}}$. The difference between the repeating and non-repeating FRBs is more obvious in terms of time-integrated luminosity than the rest-frame duration.

Upper limits on $w_{\text{int,rest}}$ are shown by triangles in Fig. 4. Since these FRBs are not temporally resolved, they might include scattered pulses if observed with a much higher time resolution. These FRBs could have much shorter $w_{\text{int,rest}}$ than the upper limit after removing the scattering component. Therefore, several temporally unresolved repeating and non-repeating FRBs (red and blue triangles in Fig. 4b, respectively) might actually overlap. However, the overall distributions of repeating and non-repeating FRBs in Fig. 4b are different, since they have different time-integrated luminosities. In terms of two distinct FRB populations in the L_ν - $w_{\text{int,rest}}$ space, the potential contributions of scattering broadening to the temporally unresolved bursts do not significantly affect our argument.

In Fig. 4, there is no clear correlation between the rest-frame duration and luminosity for repeating FRBs. This is in

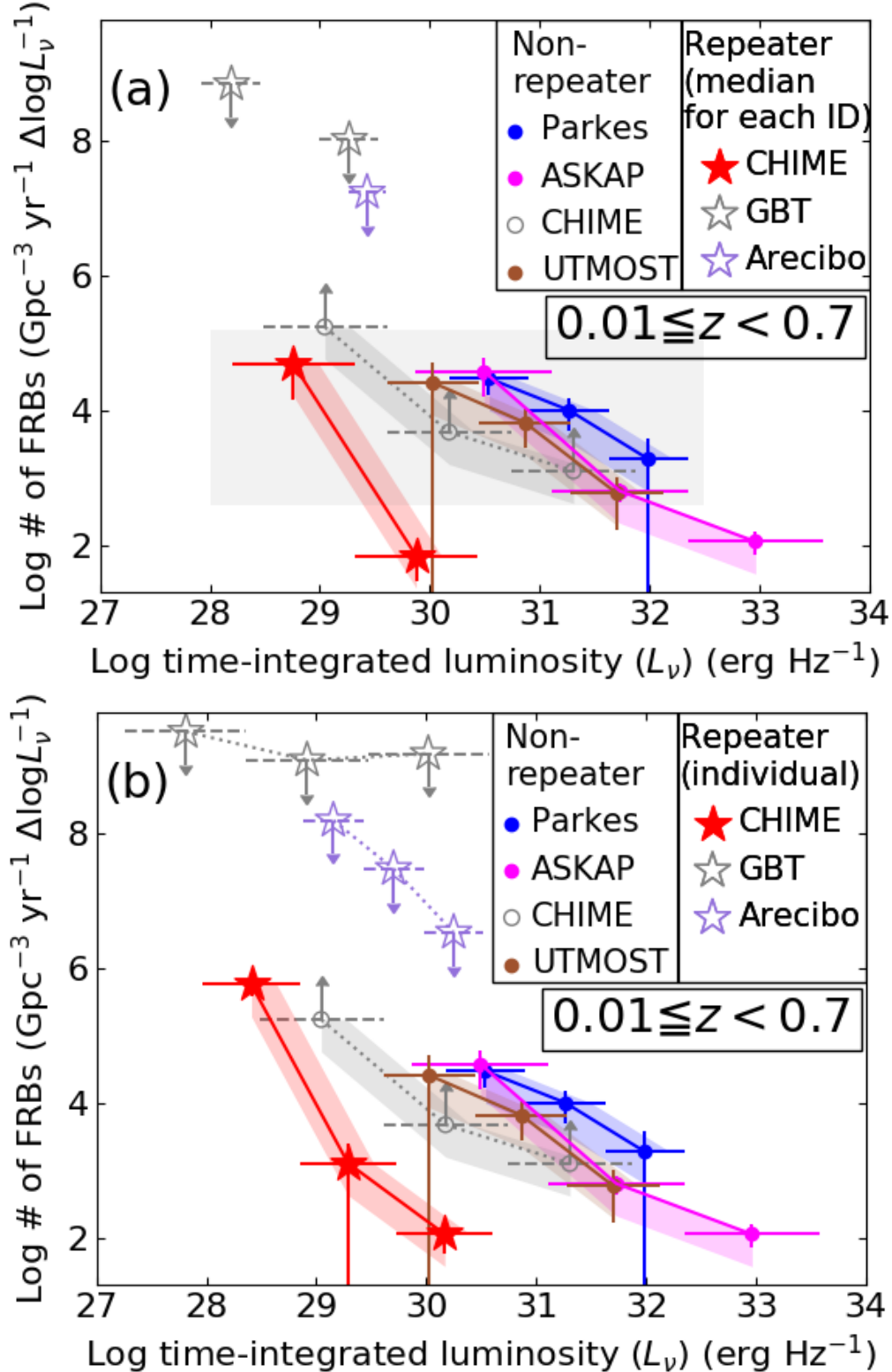


Figure 8. (Top) Luminosity function ($\log \Phi$) of FRBs. Different colours indicate different telescopes. The luminosity functions of repeating and non-repeating are shown by stars and dots, respectively. Repeating FRBs are counted such that the identical FRB ID is the single source. CHIME non-repeating FRBs place lower limits (grey open circles) because of the upper limit of the survey volume (Table 3). GBT and Arecibo FRBs place upper limits (grey and purple stars, respectively) because of targeted observations of repeating FRBs. Horizontal error bars correspond to luminosity bin sizes. Vertical error bars include the Poisson uncertainties. Upper shaded regions around the luminosity functions for Parkes, CHIME, and UTMOST correspond to systematic uncertainties in the time-integrated luminosity with respect to the unknown positions of FRBs within the fields of view. Lower shaded regions correspond to systematic uncertainties of the effective survey areas arising from the uncertainty in the slope of source counts, α_{SC} . Grey square region is magnified in Fig. 9. (Bottom) Same as top except for the different method to count the number of repeating FRBs. The repeats of bursts are individually counted for each repeating FRB.

contrast to the positive correlation found for non-repeating FRBs (Hashimoto et al. 2019). The time-integrated luminosity, i.e., a total isotropic energy released by the FRB, and duration are physically different quantities. Therefore, it is not necessary for these two quantities to be correlated even though the former is integrated over the duration. For instance, in the case of GRBs, similar parameters, E_{iso} and T_{90} , have been investigated in literature (e.g., Pélagion et al. 2008). Here, E_{iso} is the time-integrated luminosity of gamma-rays and T_{90} is the duration which includes 90% of the total gamma-ray fluence. These two physical parameters of GRBs do not show any clear correlation (Pélagion et al. 2008). Similarly, the correlation seen in the non-repeating FRB relation is not an artificial consequence from having ‘time’ in the two quantities. The detection limit depending on the observed duration, i.e., $E_{\text{lim}} \propto w_{\text{obs}}^{1/2}$, does not mimic the observed correlation (see Appendix C). Whether or not these two parameters correlate depends on the FRB models (see Section 5.3 for details). Different data distributions and non-correlation/correlation in the L_{ν} - $w_{\text{int,rest}}$ space suggest different physical origins of repeating and non-repeating FRBs.

In Fig. 5 there are, at least, two repeating FRBs which change the L_{ν} dramatically from luminous non-repeating regime to faint repeating one, i.e., FRB 171019 and 181017.J1705+68 (Kumar et al. 2019; CHIME/FRB Collaboration et al. 2019c). Kumar et al. (2019) reported repetitions of FRB 171019 which are 590 times fainter than the one discovered by ASKAP (brightest burst in Fig. 5) at different observed frequencies. In this work, the time-integrated luminosity is compared at the same frequency by assuming a spectral index measured for each repeat (Kumar et al. 2019). Therefore the difference in L_{ν} between the bright and faint repeats of FRB 171019 are larger than the factor of 590. Repeats of these two FRBs originate from the same progenitors in spite of the large L_{ν} differences. Therefore our results do not rule out a possibility that some of non-repeating FRBs are actually repeating but only the luminous repeats were detected because of sensitivity limits of telescopes.

Fig. 8 demonstrates that luminosity functions of repeating FRBs are clearly different from that of non-repeating FRBs. Even in the case of individual counting of repeats, the luminosity function of repeating FRBs is ~ 2 order of magnitude lower than that of non-repeating FRBs. The luminosity function would support the hypothesis of the different populations of repeating and non-repeating FRBs. We note that $\sim 50\%$ contamination of repeating FRBs in the non-repeating sample could mitigate the difference, since the 50% contamination decreases the number of non-repeating FRBs by 50% and increases the number of repeating FRBs up to the same level.

5.3 Implications on FRB models

A number of physical models of repeating and non-repeating FRBs have been proposed (e.g., Platts et al. 2019). Models of repeating FRBs include a neutron star-white dwarf (NS-WD) accretion (Gu et al. 2016), binary neutron-star mergers (e.g., Yamasaki et al. 2018), active galactic nuclei (AGN)-compact object interaction (e.g., Gupta & Saini 2018), AGN

jet (e.g., Katz 2017c), NS-asteroid belt interaction (Dai et al. 2016), magnetar (e.g., Beloborodov 2017; Margalit et al. 2019; Wadiasingh & Timokhin 2019; Metzger et al. 2019), pulsar lightning (Katz 2017b), starquake (Wang et al. 2018; Suvorov & Kokkotas 2019), wandering pulsar beam (Katz 2017a), and giant pulse of a young pulsar (e.g., Keane et al. 2012; Cordes & Wasserman 2016; Connor et al. 2016).

Models of non-repeating FRBs include a collapse of a neutron star (e.g., Fuller & Ott 2015; Falcke & Rezzolla 2014; Shand et al. 2016), NS-asteroid collision (Geng & Huang 2015), pulsar-black hole (BH) interaction (Bhattacharyya 2017), merger of compact objects (e.g., Zhang 2016; Liu et al. 2016; Mingarelli et al. 2015; Totani 2013; Liu 2018; Li et al. 2018; Kashiyama et al. 2013; Yamasaki et al. 2018), NS-supernova (SN) interaction (Egorov & Postnov 2009), AGN jet-cloud interaction (e.g., Romero et al. 2016) and SN remnant powered by a flare from a magnetar (e.g., Popov & Postnov 2010; Lyubarsky 2014; Murase et al. 2016).

There is no conclusive consensus on the physical origins of FRBs so far. One of the central foci of FRB studies is an observational constraint on the models. Detailed comparisons between observational results and individual physical models are beyond the scope of this work. Here we briefly sketch out rough constraints on the physical origins of repeating and non-repeating FRBs implied from observational results shown in Section 4.

The L_{ν} - $w_{\text{int,rest}}$ relation is one way to constrain the models. The observed positive correlation between L_{ν} and $w_{\text{int,rest}}$ of non-repeating FRBs could favour scenarios which predict the positive correlation with slopes similar to the observed value (Hashimoto et al. 2019). The favoured scenarios for non-repeating FRBs are, at least, (i) AGN-jet cloud interaction (e.g., Romero et al. 2016), (ii) NS-asteroid collision (e.g., Geng & Huang 2015), and (iii) SN remnant powered by a magnetar (e.g., Lyubarsky 2014), since these scenarios predict a positive correlation between L_{ν} and $w_{\text{int,rest}}$ (see Hashimoto et al. 2019, for details). As there is no clear correlation for repeating FRBs shown in Fig. 4 to 6, a possible model to explain this non-correlation is e.g. pulsar lightning (Katz 2017b).

Repeating period is another hint to constrain the repeating-FRB models. If repeating FRBs are triggered by accretion of materials (e.g., Gu et al. 2016; Katz 2017c), higher energy or brighter luminosity likely requires longer accretion time to accumulate more materials, i.e., longer period. There is no clear correlation showed in Fig. 7, though the numbers of FRBs and repeats are very small. This may rule out accretion as a possible origin mechanism of repeating FRBs. However, more future data is needed to ascertain this point.

A volumetric occurrence rate of FRBs could also provide important indication on FRB progenitors. Ravi (2019) calculated the local volumetric occurrence rate of non-repeating FRBs based on a distance to the second or third closest FRBs detected by CHIME. The rate is a lower limit because there might be other faint FRBs under the detection limit within the distance. Ravi (2019) demonstrated that the lower limit is higher than the number density of possible progenitors of FRBs and argued that most cases of non-repeating FRBs should repeat during the lifetime of the progenitors. However, only nearby two or three FRBs

are used in the analysis in spite of the detection of other FRBs. The distance to the nearby FRBs is relatively more uncertain compared to that of distant FRBs because DM_{IGM} is used as a distance indicator. The DM contamination from the Milky Way and the host galaxies become relatively larger for closer FRBs, which makes the distance to the nearby FRBs and the volumetric density more uncertain. The volumetric occurrence rate in Ravi (2019) is also very sensitive to the peculiarities of the few lowest-DM events. In addition, the number density of FRB likely depends on the luminosity as other sources in the Universe do.

In this work we used the V_{max} method to calculate volumetric occurrence rate as a function of luminosity, i.e., luminosity function of FRBs. The luminosity function contains the statistics of all FRBs at $0.01 \leq z < 0.7$ detected with each telescope, taking the detection limit and luminosity into account. In Fig. 8, the luminosity functions of CHIME-detected non-repeating FRBs (grey dots with arrows) are still lower limits because only the upper limit on the survey area of CHIME pre-commissioning observations is provided in the literature (CHIME/FRB Collaboration et al. 2019a). The grey square region in the left panel of Fig. 8 is magnified in Fig. 9 together with volumetric occurrence rates of possible progenitors (Ofek 2007; Keane & Kramer 2008; Li et al. 2011; Badenes & Maoz 2012; Taylor et al. 2014; Abbott et al. 2017; Ruiter et al. 2019; Ravi 2019). Note that the volumetric occurrence rate of each possible progenitor is integrated over luminosity. The integration of the FRB luminosity function is almost determined by the faintest bin.

In Fig. 9, the faint end of the luminosity function of the repeating FRBs detected by CHIME (red star) is comparable to those of white-dwarf mergers (Badenes & Maoz 2012), magnetars (Keane & Kramer 2008), type Ia supernovae (Li et al. 2011), and soft gamma-ray repeaters (Ofek 2007), indicating that faint repeating FRBs may be related to these progenitors. The bright end is lower than any of the possible candidates of the progenitors. The bright population of repeating FRBs is very rare, suggesting that it occurs only in an extremely small portion of the progenitors.

The faint ends of the luminosity functions of non-repeating FRBs detected with Parkes, ASKAP, and UTMOST (faint ends of blue, magenta, and brown dots in Fig. 9) are comparable to that of repeating FRBs (red star) and thus have similar rates to white-dwarf mergers (Badenes & Maoz 2012), magnetars (Keane & Kramer 2008), type Ia supernovae (Li et al. 2011), and soft gamma-ray repeaters (Ofek 2007). The faint ends are higher than those of neutron-star mergers (Abbott et al. 2017) and accretion-induced collapse of white dwarfs (Moriya 2016; Ruiter et al. 2019). There are two possibilities, i.e., either (i) faint non-repeating FRBs originate in neutron-star mergers or accretion-induced collapse and are actually repeating during the lifetime of the progenitor or (ii) faint non-repeating FRBs are 'truly non-repeating' without significant contamination from repeaters and do not originate in either neutron-star mergers or accretion-induced collapse. The case (i) is consistent with the discussion presented in Ravi (2019). There might be contamination of repeating FRBs in the non-repeating ones. The case (ii) could indicate that the progenitors of faint non-repeating FRBs are any of soft gamma-ray repeaters, type Ia supernovae, magnetars, and white-dwarf mergers in terms of the volumetric occurrence rate. The bright end of

the luminosity function of the non-repeating FRBs is lower than any of the possible candidates of the progenitors. The bright non-repeating FRBs might also originate in a very small fraction of the possible progenitors. Otherwise, bright FRBs might originate in unknown progenitors.

These statistical arguments are based on only the rate matching analysis. More direct evidences would be obtained via follow-up observations of the possible progenitors. Although radio follow-up observations of the possible progenitors, e.g., GRBs (Madison et al. 2019; Men et al. 2019) and supernova remnants (Law et al. 2019) have not yet detected any FRB counterparts so far, direct detection of FRBs from them are necessary to give a more comprehensive answer to the FRB origins.

6 CONCLUSIONS

We compiled a total of 11 repeating FRBs with 144 repeats and 77 non-repeating FRBs from the FRBCAT project. From this sample we found that repeating and non-repeating FRBs are clearly distinguishable in the L_{ν} - $w_{\text{int,rest}}$ parameter space (Fig. 4), where L_{ν} and $w_{\text{int,rest}}$ are the time-integrated luminosity and rest-frame intrinsic duration of FRBs, respectively. The repeating FRBs have fainter L_{ν} and longer $w_{\text{int,rest}}$ compared to the non-repeating population. In contrast to non-repeating FRBs, repeating FRBs do not show any clear correlation between the L_{ν} and $w_{\text{int,rest}}$. We also found that the luminosity function of repeating FRBs is much lower than that of non-repeating FRBs (Fig. 8). These results imply that repeating and non-repeating FRBs are essentially different populations.

During the repeats of FRBs, each repeat randomly moves in the L_{ν} - $w_{\text{int,rest}}$ plane without any clear trend (Figs. 5 and 6). Physical models which do not predict any correlation between the L_{ν} and $w_{\text{int,rest}}$ could be favoured for repeating FRBs, e.g., a pulsar lightning scenario. Accretion-material scenario might be disfavoured for repeating FRBs, since we do not find any clear correlation between the cadence and time-integrated luminosity (Fig. 7).

The faint ends of the luminosity functions of repeating and non-repeating FRBs are higher than volumetric occurrence rates of neutron-star mergers and accretion-induced collapse of white dwarfs (Fig. 9). They are consistent with the rates of soft gamma-ray repeaters, type Ia supernovae, magnetars, and white-dwarf mergers. This indicates two possibilities: either (i) faint non-repeating FRBs originate in neutron-star mergers or accretion-induced collapse and are actually repeating during the lifetime of the progenitor or (ii) faint non-repeating FRBs are not related to these possible progenitors but originate in any of soft gamma-ray repeaters, type Ia supernovae, magnetars, and white-dwarf mergers.

The bright ends of luminosity functions of repeating and non-repeating FRBs are lower than any candidates of progenitors (Fig. 9). This suggests that bright FRBs are extremely rare and are produced from a very small fraction of the progenitors regardless of the repetition. Otherwise, bright FRBs might originate in unknown progenitors.

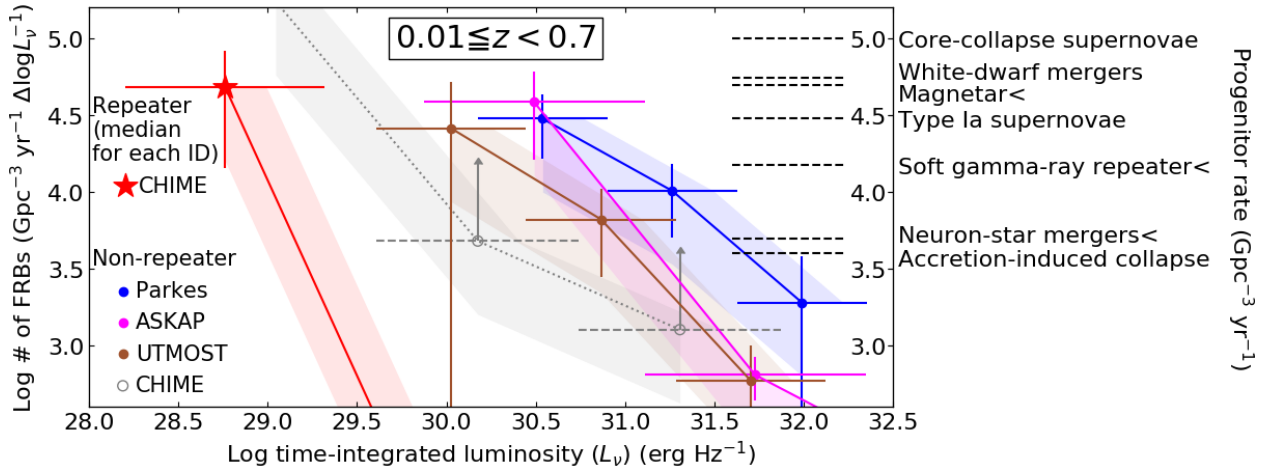


Figure 9. Magnified figure of the grey square region in Fig. 8 (a), comparing with possible progenitors' volumetric occurrence rates (Ofek 2007; Keane & Kramer 2008; Li et al. 2011; Badenes & Maoz 2012; Taylor et al. 2014; Abbott et al. 2017; Ruiter et al. 2019; Ravi 2019). The rates of magnetar, soft gamma-ray repeater, and neutron-star mergers correspond to the upper limits (Ofek 2007; Keane & Kramer 2008; Abbott et al. 2017). Repeating FRBs are counted such that the identical FRB ID is the single source. Upper shaded regions around the luminosity functions for Parkes, CHIME, and UTMOST correspond to systematic uncertainties with respect to the unknown positions of FRBs within the fields of view. Lower shaded regions correspond to systematic uncertainties of the effective survey areas arising from the uncertainty in the slope of source counts, α_{SC} .

ACKNOWLEDGEMENTS

We are very grateful to the anonymous referee for many insightful comments. TH and AYLO are supported by the Centre for Informatics and Computation in Astronomy (CICA) at National Tsing Hua University (NTHU) through a grant from the Ministry of Education of the Republic of China (Taiwan). TG acknowledges the support by the Ministry of Science and Technology of Taiwan through grant 108-2628-M-007-004-MY3. AYLO's visit to NTHU was supported by the Ministry of Science and Technology of the ROC (Taiwan) grant 105-2119-M-007-028-MY3, hosted by Prof. Albert Kong. This work made use of the CICA Cluster at the NTHU/CICA, supported by the Taiwan Ministry of Education and NTHU. This research has made use of NASA's Astrophysics Data System.

REFERENCES

Aartsen M. G., et al., 2020, *ApJ*, **890**, 111
 Abbott B. P., et al., 2017, *Phys. Rev. Lett.*, **119**, 161101
 Avni Y., Bahcall J. N., 1980, *ApJ*, **235**, 694
 Badenes C., Maoz D., 2012, *ApJ*, **749**, L11
 Bannister K. W., et al., 2017, *ApJ*, **841**, L12
 Bannister K. W., et al., 2019, *Science*, **365**, 565
 Beloborodov A. M., 2017, *ApJ*, **843**, L26
 Bhattacharyya S., 2017, arXiv e-prints,
 CHIME/FRB Collaboration et al., 2019a, *Nature*, **566**, 230
 CHIME/FRB Collaboration et al., 2019b, *Nature*, **566**, 235
 CHIME/FRB Collaboration et al., 2019c, *ApJ*, **885**, L24
 Caleb M., et al., 2016, *MNRAS*, **458**, 718
 Caleb M., et al., 2017, *MNRAS*, **468**, 3746
 Callister T., Kanner J., Weinstein A., 2016, *ApJ*, **825**, L12
 Connor L., Sievers J., Pen U.-L., 2016, *MNRAS*, **458**, L19
 Cordes J. M., Lazio T. J. W., 2002, arXiv e-prints, pp astro-ph/0207156
 Cordes J. M., Wasserman I., 2016, *MNRAS*, **457**, 232

Dai Z. G., Wang J. S., Wu X. F., Huang Y. F., 2016, *ApJ*, **829**, 27
 Dolag K., Gaensler B. M., Beck A. M., Beck M. C., 2015, *MNRAS*, **451**, 4277
 Egorov A. E., Postnov K. A., 2009, *Astronomy Letters*, **35**, 241
 Falcke H., Rezzolla L., 2014, *A&A*, **562**, A137
 Farah W., et al., 2019, *MNRAS*, **488**, 2989
 Fedorova V. A., Rodin A. E., 2019, *Astronomy Reports*, **63**, 39
 Fuller J., Ott C. D., 2015, *MNRAS*, **450**, L71
 Geng J. J., Huang Y. F., 2015, *ApJ*, **809**, 24
 Gu W.-M., Dong Y.-Z., Liu T., Ma R., Wang J., 2016, *ApJ*, **823**, L28
 Gupta P. D., Saini N., 2018, *Journal of Astrophysics and Astronomy*, **39**, 14
 Hashimoto T., Goto T., Wang T.-W., Kim S. J., Wu Y.-H., Ho C.-C., 2019, *MNRAS*, **488**, 1908
 Kashiyama K., Ioka K., Mészáros P., 2013, *ApJ*, **776**, L39
 Katz J. I., 2017a, *MNRAS*, **467**, L96
 Katz J. I., 2017b, *MNRAS*, **469**, L39
 Katz J. I., 2017c, *MNRAS*, **471**, L92
 Keane E. F., Kramer M., 2008, *MNRAS*, **391**, 2009
 Keane E. F., Petroff E., 2015, *MNRAS*, **447**, 2852
 Keane E. F., Stappers B. W., Kramer M., Lyne A. G., 2012, *MNRAS*, **425**, L71
 Keating L. C., Pen U.-L., 2020, arXiv e-prints, p. arXiv:2001.11105
 Kumar P., et al., 2019, *ApJ*, **887**, L30
 Law C. J., et al., 2019, *ApJ*, **886**, 24
 Li W., Chornock R., Leaman J., Filippenko A. V., Poznanski D., Wang X., Ganeshalingam M., Mannucci F., 2011, *MNRAS*, **412**, 1473
 Li L.-B., Huang Y.-F., Geng J.-J., Li B., 2018, *Research in Astronomy and Astrophysics*, **18**, 061
 Liu X., 2018, *Ap&SS*, **363**, 242
 Liu T., Romero G. E., Liu M.-L., Li A., 2016, *ApJ*, **826**, 82
 Lorimer D. R., Bailes M., McLaughlin M. A., Narkevic D. J., Crawford F., 2007, *Science*, **318**, 777
 Luo R., Lee K., Lorimer D. R., Zhang B., 2018, *MNRAS*, **481**, 2320
 Lyubarsky Y., 2014, *MNRAS*, **442**, L9

MAGIC Collaboration et al., 2018, *MNRAS*, **481**, 2479
 Macquart J. P., Ekers R. D., 2018, *MNRAS*, **474**, 1900
 Macquart J.-P., Shannon R. M., Bannister K. W., James C. W., Ekers R. D., Bunton J. D., 2019, *ApJ*, **872**, L19
 Madison D. R., et al., 2019, *ApJ*, **887**, 252
 Marcote B., et al., 2020, *Nature*, **577**, 190
 Margalit B., Berger E., Metzger B. D., 2019, *ApJ*, **886**, 110
 Martone R., et al., 2019, *A&A*, **631**, A62
 Men Y., et al., 2019, *MNRAS*, **489**, 3643
 Metzger B. D., Margalit B., Sironi L., 2019, *MNRAS*, **485**, 4091
 Michilli D., et al., 2018, *Nature*, **553**, 182
 Mingarelli C. M. F., Levin J., Lazio T. J. W., 2015, *ApJ*, **814**, L20
 Moriya T. J., 2016, *ApJ*, **830**, L38
 Murase K., Kashiyama K., Mészáros P., 2016, *MNRAS*, **461**, 1498
 Ofek E. O., 2007, *ApJ*, **659**, 339
 Osłowski S., et al., 2019, *MNRAS*, **488**, 868
 Pélagion A., et al., 2008, *A&A*, **491**, 157
 Petroff E., et al., 2016, *Publ. Astron. Soc. Australia*, **33**, e045
 Planck Collaboration et al., 2016, *A&A*, **594**, A13
 Platts E., Weltman A., Walters A., Tendulkar S. P., Gordin J. E. B., Kandhai S., 2019, *Phys. Rep.*, **821**, 1
 Popov S. B., Postnov K. A., 2010, in Harutyunian H. A., Mickaelian A. M., Terzian Y., eds, *Evolution of Cosmic Objects through their Physical Activity*. pp 129–132 ([arXiv:0710.2006](https://arxiv.org/abs/0710.2006))
 Prochaska J. X., Zheng Y., 2019, *MNRAS*, **485**, 648
 Prochaska J. X., et al., 2019, *Science*, **365**, aay0073
 Ravi V., 2019, *Nature Astronomy*, **3**, 928
 Ravi V., et al., 2019, *Nature*, **572**, 352
 Romero G. E., del Valle M. V., Vieyro F. L., 2016, *Phys. Rev. D*, **93**, 023001
 Ruiter A. J., Ferrario L., Belczynski K., Seitzzahl I. R., Crocker R. M., Karakas A. I., 2019, *MNRAS*, **484**, 698
 Schmidt M., 1968, *ApJ*, **151**, 393
 Scholz P., et al., 2016, *ApJ*, **833**, 177
 Shand Z., Ouyed A., Koning N., Ouyed R., 2016, *Research in Astronomy and Astrophysics*, **16**, 80
 Shannon R. M., et al., 2018, *Nature*, **562**, 386
 Spitler L. G., et al., 2014, *ApJ*, **790**, 101
 Spitler L. G., et al., 2016, *Nature*, **531**, 202
 Spitler L. G., et al., 2018, *ApJ*, **863**, 150
 Sun S., Yu W., Yu Y., Mao D., Lin J., 2019, *ApJ*, **885**, 55
 Suvorov A. G., Kokkotas K. D., 2019, *MNRAS*, **488**, 5887
 Taylor M., et al., 2014, *ApJ*, **792**, 135
 Tendulkar S. P., et al., 2017, *ApJ*, **834**, L7
 Tingay S. J., Yang Y.-P., 2019, *ApJ*, **881**, 30
 Totani T., 2013, *PASJ*, **65**, L12
 Wadiasingh Z., Timokhin A., 2019, *ApJ*, **879**, 4
 Wang W., Luo R., Yue H., Chen X., Lee K., Xu R., 2018, *ApJ*, **852**, 140
 Yamasaki S., Totani T., Kiuchi K., 2018, *PASJ*, **70**, 39
 Yao J. M., Manchester R. N., Wang N., 2017, *ApJ*, **835**, 29
 Zhang B., 2016, *ApJ*, **827**, L31
 Zhang Y. G., Gajjar V., Foster G., Siemion A., Cordes J., Law C., Wang Y., 2018, *ApJ*, **866**, 149
 Zhang S. B., Hobbs G., Dai S., Toomey L., Staveley-Smith L., Russell C. J., Wu X. F., 2019, *MNRAS*, **484**, L147
 Zhou B., Li X., Wang T., Fan Y.-Z., Wei D.-M., 2014, *Phys. Rev. D*, **89**, 107303
 Zhu W., Feng L.-L., Zhang F., 2018, *ApJ*, **865**, 147

APPENDIX A: DM_{IGM} AND REDSHIFT DISTRIBUTION IN EACH TELESCOPE

Fig. 1 includes the contributions from a variety of telescopes with different survey sensitivities and DM distributions. In Figs. A1 and A2, we show the distributions of DM_{IGM} and redshift of each telescope in our sample, respectively.

APPENDIX B: DETECTION LIMITS DEPENDING ON DURATION

Here we empirically estimate a detection limit, E_{lim} , for each telescope. Fig. B1 shows the observed duration as a function of observed fluence. Each panel indicates FRBs detected with each telescope. Dashed lines correspond to detection limits reported in previous works (Spitler et al. 2014; Keane & Petroff 2015; Caleb et al. 2016; Shannon et al. 2018; CHIME/FRB Collaboration et al. 2019a). The reported detection limits of ASKAP, CHIME, and Arecibo include the duration dependency explicitly, while those of Parkes and UTMOST do not. The different definitions of the detection limit could introduce additional systematics in different telescopes. To remove such systematics, we adopt the same definition of the detection limit that involves the $w_{\text{obs}}^{1/2}$ dependency. For each telescope, we approximated E_{lim} as a peak of data distribution along the perpendicular direction to the $w_{\text{obs}}^{1/2}$ dependency in Fig. B1. The peak is utilised to reduce the uncertainty with respect to observational incompleteness. In order to investigate the peak of data distribution, Fig. B1 was rotated so that the $w_{\text{obs}}^{1/2}$ dependency can be aligned along the vertical axis (Fig. B2). The peaks of histograms in Fig. B2 correspond to empirically determined E_{lim} as shown by the black solid lines in Figs. B1 and B2.

APPENDIX C: DOES DETECTION LIMIT MIMIC THE LUMINOSITY-DURATION RELATION?

We performed Monte Carlo simulations to confirm whether the detection limits of radio telescopes, $E_{\text{lim}} \propto w_{\text{obs}}^{1/2}$, mimic the L_{ν} - $w_{\text{int,rest}}$ correlation found for non-repeating FRBs. In each simulation, we assumed 120 artificial data uniformly-distributed in the L_{ν} - $w_{\text{int,rest}}$ plane ranging from $\log(L_{\nu}) = 30.0$ to 34.0 (erg Hz^{-1}) and $\log(w_{\text{int,rest}}) = -1.0$ to 1.5 (ms). This artificial data distribution has no ‘intrinsic’ correlation, but the correlation coefficient slightly fluctuates due to the random process. For the artificial redshift distribution, we used the best-fit Gaussian function to the redshift distribution of FRBs detected with Parkes, i.e., a Gaussian function centred at $z = 0.86$ with $\sigma = 0.6$. The redshift is randomly assigned to each artificial data following this Gaussian probability distribution function. We also randomly assigned galactic coordinates, b and l , to each data because DM_{MW} and thus DM_{obs} affects w_{obs} through the dispersion smearing. Among 120 artificial data, each of the four telescopes -Parkes, ASKAP, CHIME, and UTMOST- will observed 30 artificial data points. For each telescope, median values of w_{sample} , ν_{obs} , and $\Delta\nu_{\text{obs}}$ in our sample are utilised, where w_{sample} , ν_{obs} , and $\Delta\nu_{\text{obs}}$ are the sampling time, observed frequency, and intra-channel bandwidth, respectively. Based on

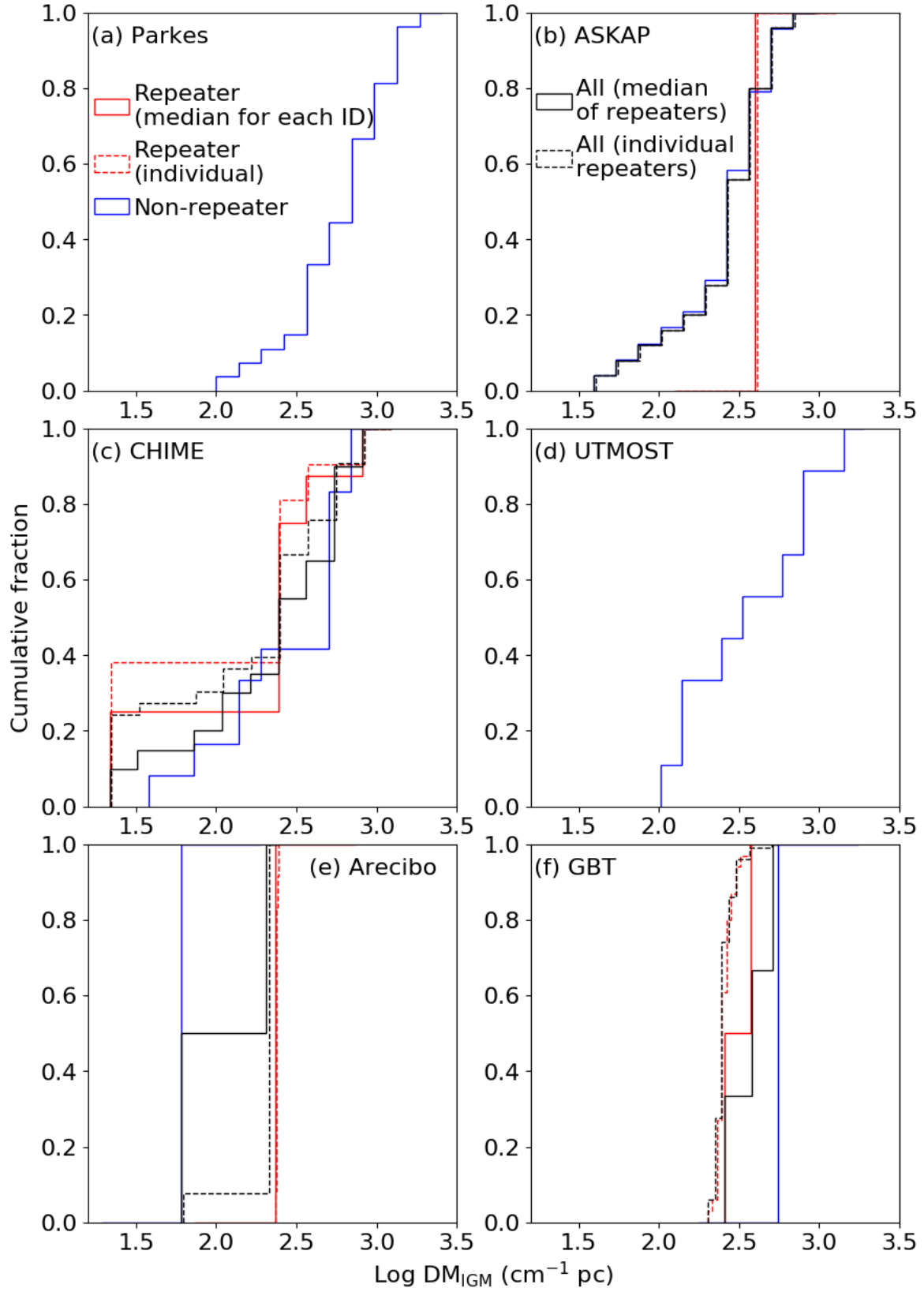


Figure A1. Same as Fig. 1e except for plotting samples of individual telescopes.

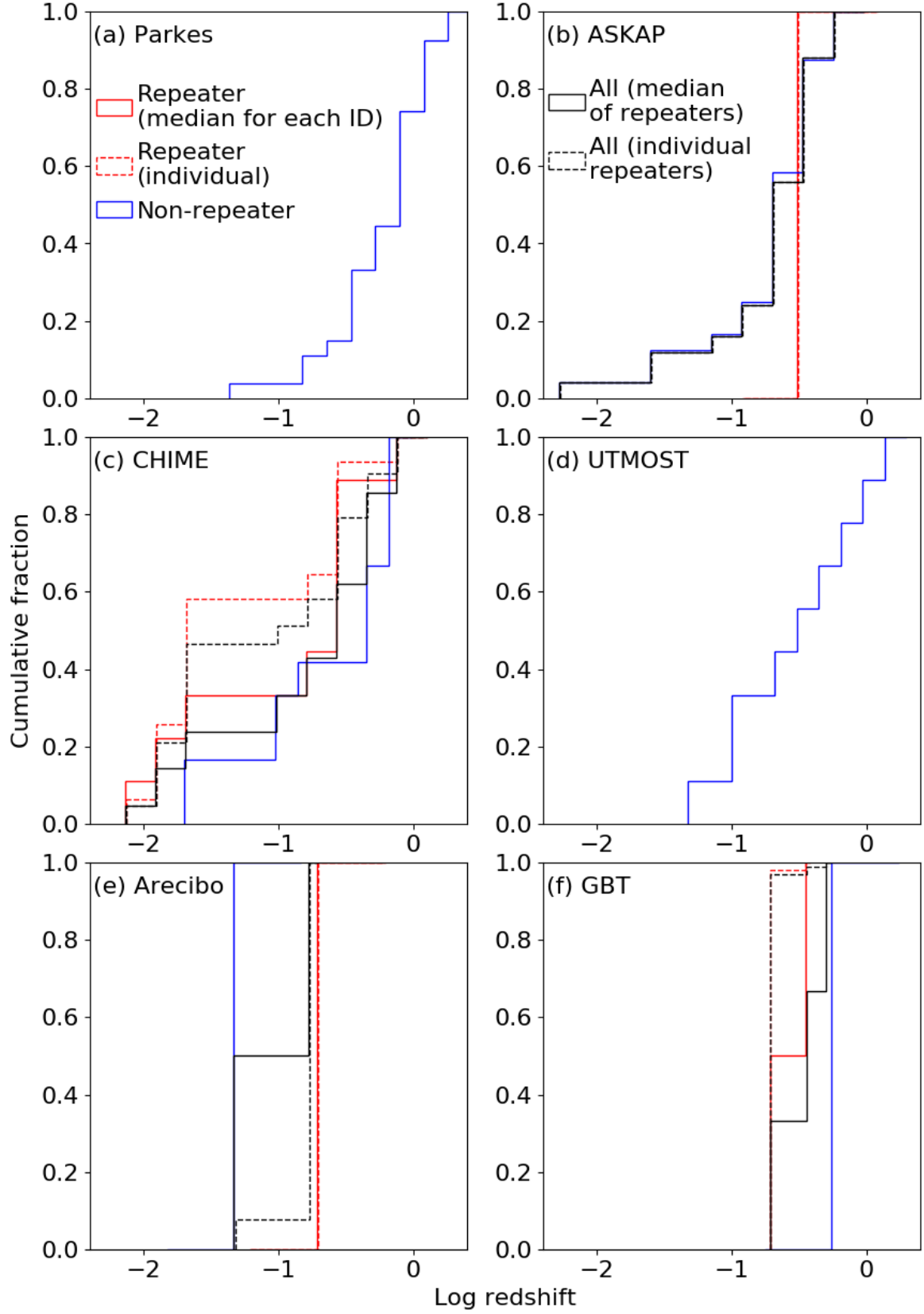


Figure A2. Same as Fig. 1f except for plotting samples of individual telescopes.

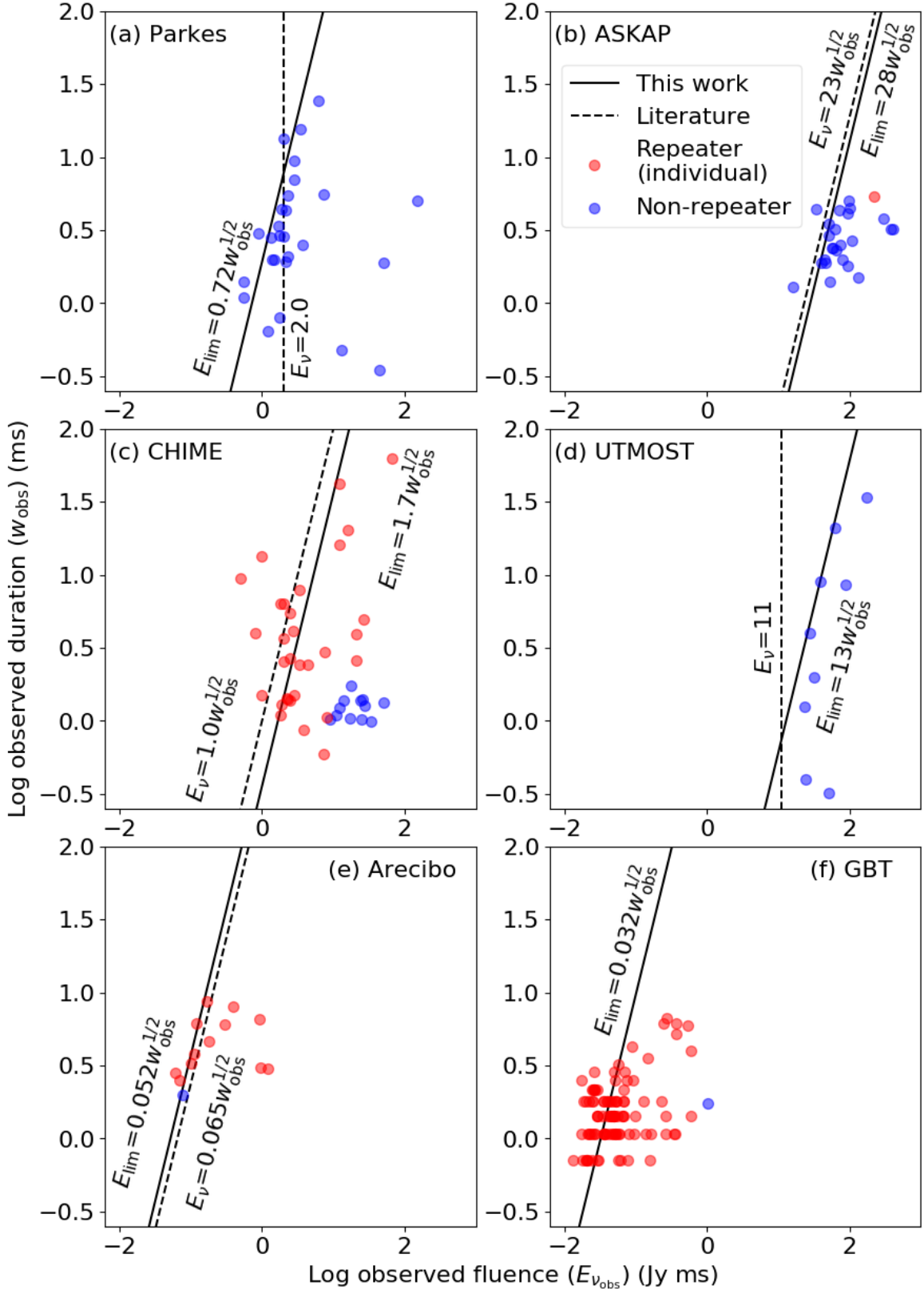


Figure B1. Observed duration as a function of fluence of our FRB sample. Each panel indicates data obtained by each telescope. Red and blue dots correspond to repeating and non-repeating FRBs, respectively. Solid lines are detection limits that we empirically calculated (see also Fig. B2). Dashed lines are detection limits reported in literature (Spitler et al. 2014; Keane & Petroff 2015; Caleb et al. 2016; Shannon et al. 2018; CHIME/FRB Collaboration et al. 2019a). All of our sample is demonstrated before applying the redshift cuts and detection limits for the calculations of luminosity functions.

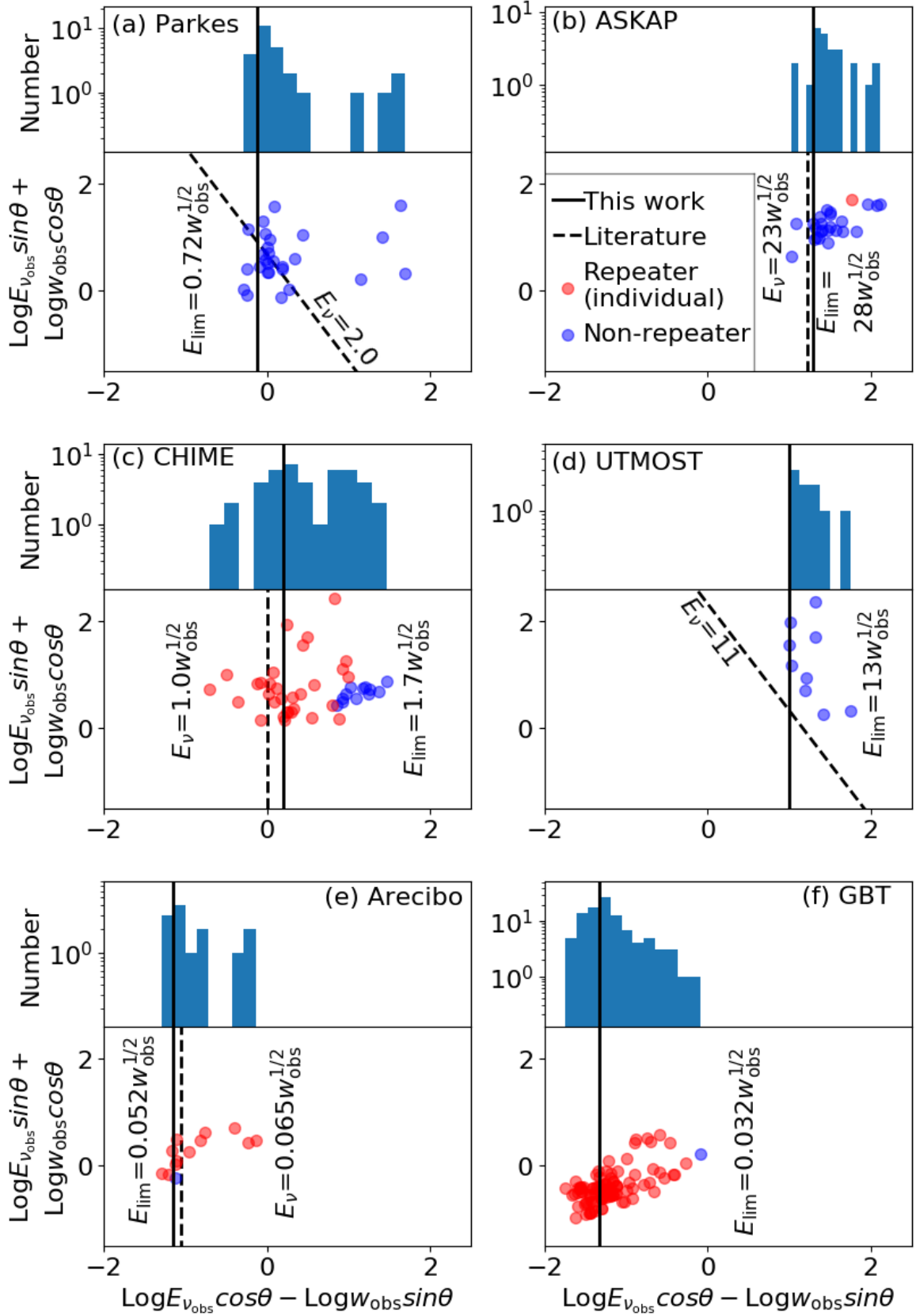


Figure B2. Same as Fig. B1 except for rotation of the axes. The axes are rotated so that the duration dependency on the detection limit can be aligned along the vertical axis. Top figure in each panel shows a histogram of FRBs including repeating and non-repeating ones detected with each telescope. The rotation angle, θ , is $\pi/2 - \tan^{-1}(2.0)$ rad. The detection limits in our analysis are determined by the peaks of the histograms.

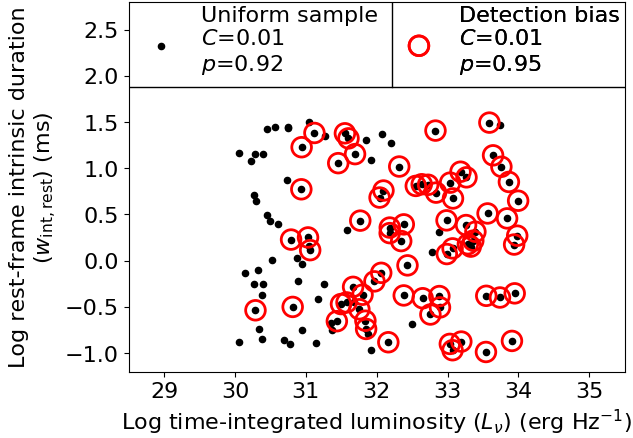


Figure C1. One example of the Monte Carlo simulations. Black dots are 120 simulated data following a uniform probability distribution in the L_ν - $w_{\text{int,rest}}$ plane. Four radio telescopes - Parkes, ASKAP, CHIME and UTMOST - are supposed to observe each 30 simulated data based on our detection limits (see also Figs. B1 and B2). The detected sources are marked by red circles. We iterated this process 10,000 times to derive histograms of Pearson coefficients (C) and p -values (p) in Fig. C2, where C and p indicate the strength of correlation and statistical significance, respectively. This example indicates no significant correlation between L_ν and $w_{\text{int,rest}}$ in the intrinsic uniform data distribution and detected FRBs.

these assumptions, we calculated the observed quantities, E_{obs} and w_{obs} , following the methods described in Sections 3.1 and 3.2. We here define ‘detected FRBs’ if E_{obs} is higher than $E_{\text{lim}}(\propto w_{\text{obs}}^{1/2})$. E_{lim} is empirically determined for each telescope (see Appendix B).

Fig. C1 shows an example of a simulation with 120 artificial data points. In this example, a Pearson coefficient (C) and p -value (p) are $C = 0.01$ and $p = 0.92$ for the intrinsic uniform data distribution, whereas $C = 0.01$ and $p = 0.95$ for the detected FRBs. C and p indicate the strength of correlation and statistical significance, respectively. These values indicate no significant correlation between L_ν and $w_{\text{int,rest}}$ in the intrinsic uniform data distribution and detected FRBs.

We iterated this 120-data simulation 10,000 times. The histograms of Pearson coefficients and p -values are shown in Fig. C2. In Fig. C2a, we found that the peak position of Pearson coefficients moved from $C = 0.0$ to ~ 0.1 after the detection limits are applied. This value of $C \sim 0.1$ is much smaller than the observed one, i.e., $C \sim 0.5$ (Hashimoto et al. 2019). In Fig. C2b, 97.3% of cases among 10,000 iterations indicate no significant correlation between L_ν and $w_{\text{int,rest}}$. Therefore, we conclude that the duration-dependent detection limit does not mimic a statistically significant correlation.

This paper has been typeset from a \LaTeX file prepared by the author.

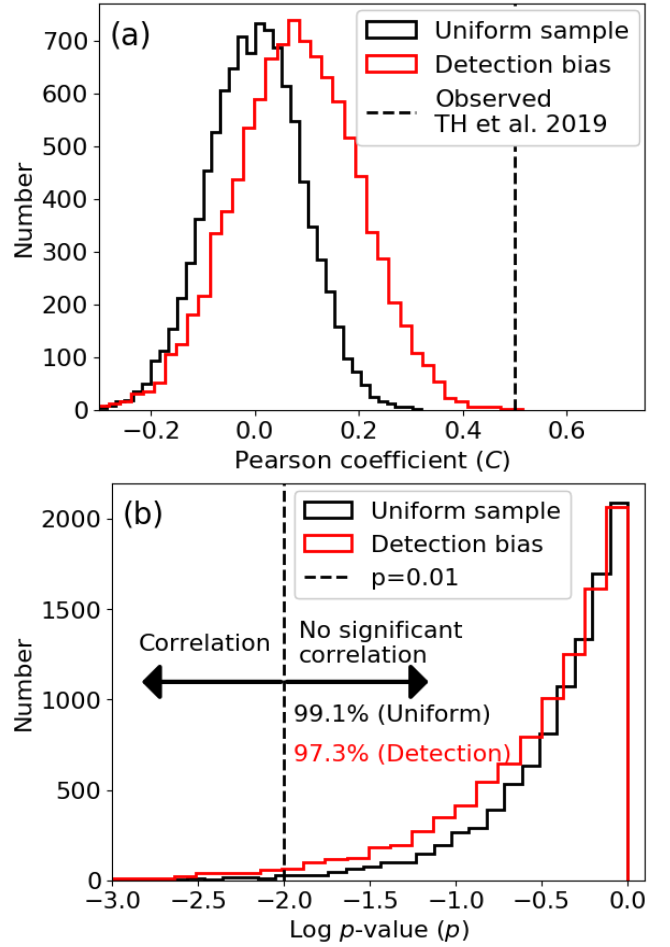


Figure C2. Histograms of (Top) Pearson coefficients and (Bottom) p -values derived from the Monte Carlo simulation. The histograms of the original uniform sample are shown by black solid lines and those of detected sources are shown in red. Dashed vertical lines in the top and bottom panels correspond to a coefficient measured for the observed FRB sample in Hashimoto et al. (2019) and $p=0.01$, respectively.